Int J Earth Sci (Geol Rundsch) (2017) 106:453–476
DOI 10.1007/s00531-016-1417-x

ORIGINAL PAPER

Timing and duration of partial melting and magmatism in the Variscan Montagne Noire gneiss dome (French Massif Central)

Pierre Trap[1] · Françoise Roger[2] · Bénédicte Cenki-Tok[2] · Jean-Louis Paquette[3]

Received: 11 January 2016 / Accepted: 16 October 2016 / Published online: 19 November 2016

Abstract Unravelling the detailed pressure–temperature–time-deformation (P–T–t-D) evolution of magmatic and metamorphic rocks provides essential insights into the timing and duration of partial melting and related plutonism during crustal flow and migmatitic dome formation. The Montagne Noire Axial Zone (MNAZ) is a migmatitic dome located within the Variscan orogen in the southern French Massif Central. The timing of the main thermal event that was responsible for intense partial melting is still highly debated. In this study we present new laser ablation inductively coupled plasma mass spectrometry (LA-ICP-MS) age data on micaschists, migmatites and granites that clarify the P–T–t-D evolution of the MNAZ. Structurally controlled samples were collected in order to constrain the timing of metamorphism, migmatization and plutonism regarding the main structural pattern D1, D2 and D3. D1 and D2 correspond to nappe stacking and dextral transpression, respectively. D3 is related to vertical shortening and coaxial thinning with a preferential NE–SW- to E–W-directed stretching. LA-ICP-MS analyses on the syntectonic Anglès, Soulié and Martys granites yielded U–Th/Pb monazite ages of 305 ± 1.5, 306 ± 1.9 and 314 ± 2 Ma, respectively. Five migmatitic rocks sampled in the eastern and central Espinouse area yielded in situ ages ranging between 312 ± 2 and 301 ± 2 Ma. Along the dome envelope, two garnet–staurolite-bearing micaschists near Saint-Pons-de-Thomières village gave in situ U–Th–Pb ages of 312.1 ± 2.1 and 309.0 ± 3.1 Ma. A fine-grained gneiss with a D3 fabrics in the eastern dome envelope yield a $^{208}Pb/^{232}Th$ mean age at 305.7 ± 3.9 Ma. All ages obtained in this study for the micaschists, migmatites and granites range between 315 and 301 Ma. We interpret this time span as the record of the high thermal event responsible for intense crustal partial melting within the lower and middle crust. The onset of partial melting occurred at ca. 315 Ma that marked the beginning of transpressional deformation D2. Based on structural and petrological studies, our new U–Th–Pb results suggest that (1) partial melting may have started at ca. 315 Ma and lasted 15–10 Myr and (2) D2 et D3 developed between 315 and 300 Ma and were synchronous. D1 deformation ended at 315 Ma. The onset and duration of D1 related to nappe stacking and crustal thickening is still uncertain.

Keywords Partial melting · Migmatite · Magmatism · Variscan orogeny · Gneiss dome · LA-ICP-MS U–Th–Pb dating

Electronic supplementary material The online version of this article (doi:10.1007/s00531-016-1417-x) contains supplementary material, which is available to authorized users.

✉ Pierre Trap
pierre.trap@univ-fcomte.Fr

[1] Laboratoire Chrono-environnement (CNRS-UMR 6249), Université de Bourgogne-Franche-Comté, 16 route de Gray, 25030 Besançon Cedex, France

[2] Laboratoire Géosciences Montpellier (CNRS-UMR 5243), Université de Montpellier, Place Eugène Bataillon, 34095 Montpellier Cedex 5, France

[3] Laboratoire Magmas et Volcans (CNRS-UMR 6524), Université Blaise Pascal, 6 Avenue Blaise Pascal, 63038 Clermont-Ferrand Cedex, France

Introduction

Within the European Variscan belt, crustal partial melting and magmatism were intense and widespread, in particular during Carboniferous times (e.g. Faure et al. 2009, 2010; Lardeaux

2014) with a significant rheological impact on orogenic dynamics and crustal flow (Vanderhaeghe and Teyssier 2001; Vanderhaeghe et al. 1999). The flow of the partially molten crust documented during Carboniferous times is regarded as an analogue to what is observed in actual orogenic plateau like the Andes (e.g. Guy et al. 2011; Schulmann et al. 2009). Unravelling the spatial distribution and timing of partial melting within the mature Variscan crust may give important insights into flow mechanisms acting inside orogenic plateaus. However, several important questions remain unresolved or highly debated: (1) is partial melting of the crust synchronous at the scale of the whole belt (i.e. in the internal or external zone) or is it diachronous and localized? (2) What is the relationship between partial melting and the tectono-metamorphic evolution, i.e. is it syn-, late or post-orogenic? (3) What is the duration of partial melting events?

Within the Variscan French Massif Central, deciphering the origin of heat sources for metamorphism and partial melting at the scale of the entire orogenic belt is an additional issue. Faure et al. (2010) proposed that subsequent to the amalgamation of continental masses during Early Carboniferous times, the lithospheric mantle was thinned and an important heat transfer from the asthenosphere triggered melting of the lower and middle crust throughout the entire belt.

Within the external domain of the belt, in the Montagne Noire massif, an ambiguity persists about the timing of the main thermal event that was responsible for intense partial melting. It occurred around to 335–320 Ma (Faure et al. 2010, 2014) or 315–300 Ma (Roger et al. 2015; Whitney et al. 2015). This debate about timing of metamorphism also exists for the early HP metamorphic event (M1) coeval with crustal thickening: were eclogitic conditions reached at 360 Ma (Faure et al. 2014) or at 315 Ma (Whitney et al. 2015)? Constraining the timing and duration of partial melting and the prograde history of the terrane is a very challenging task that demands a clear understanding of the structural and metamorphic settings.

In this contribution, we present new geochronological data on 12 samples (micaschists, migmatites and granites) from the Montagne Noire Axial Zone (MNAZ) in the southern part of the French Massif Central. These geochronological results are interpreted in the light of the new structural and petrological data proposed by Rabin et al. (2015) and Fréville et al. (2016). Finally, a semi-quantitative P–T–t-D evolution for rocks of the MNAZ is proposed. The geodynamic implications of these results are discussed within the framework of the tectonic evolution of the Variscan belt.

Geological setting

The Montagne Noire massif is located at the southernmost edge of the French Central Massif, which consists of a stack of tectonic slices from bottom to top, the para-autochthonous Unit, the Lower Gneiss Unit and the Upper Gneiss Unit, (e.g. Ledru et al. 1989; Faure et al. 2009; Franke et al. 2011; Lardeaux 2014) (Fig. 1a). The southern external zone of the Variscan belt is made of a Paleozoic fold-and-thrust belt bounded to the south by a Visean–Namurian foreland turbiditic basin (Franke et al. 2011; Faure et al. 2009; Engel et al. 1978, 1980; Feist and Galtier 1985).

The Montagne Noire massif is subdivided in two main domains (Fig. 1b). The first domain corresponds to the upper structural level. It includes the northern and southern flanks that both consist in a nappe stack of imbricated Paleozoic low grade to unmetamorphosed sedimentary rocks (Fig. 1b) (Gèze 1949; Arthaud 1970; Aerden 1998; Demange 1996, 1998; Doublier et al. 2014). The second domain, the MNAZ, corresponds to the lower structural part. It is made of gneisses and migmatites forming a gneiss dome mantled by an upper Proterozoic to Ordovician metasedimentary cover (Demange 1993, 1994; Franke et al. 2011). Numerous late orogenic granites intrude this sequence (Fig. 1b). According to Faure et al. (2010) migmatization and emplacement of anatectic granitoids took place at around 333–326 Ma and post-migmatitic granitoids emplaced around 325–318 Ma. More recently, Roger et al. (2015) suggested that high-temperature metamorphism and plutonism occurred between 315 and 300 Ma. The MNAZ also includes a few localities in which mafic pods displaying eclogite facies assemblage occur (Demange 1985; Faure et al. 2014; Whitney et al. 2015). The processes leading to the exhumation of the MNAZ high-grade core have been debated for many decades. Different authors have emphasized tectonic processes involving diapirism (Gèze 1949; Schuiling 1960; Faure et al. 2010) or contraction/transpression (Arthaud 1970; Matte et al. 1998; Demange 1999; Malavieille 2010), strike–slip (Nicolas et al. 1977; Franke et al. 2011), or extension/transtension (Van den Driessche and Brun 1989, 1992; Echtler and Malavieille 1990; Brun and Van den Driessche 1994, 1996; Rey et al. 2011, 2012).

Lithological outlines of the MNAZ

The MNAZ is a NE–SW trending gneiss dome made of four main lithological units: (1) schist and micaschist, (2) migmatitic orthogneiss, (3) metapelitic metatexite and (4) diatexite and granite (Fig. 1b). The schist and micaschist units consist predominantly in metapelitic sequences that show a progressive increase in metamorphic conditions from greenschist facies conditions (sericite–chlorite-bearing schists), to amphibolite conditions (kyanite–staurolite schists) and andalusite–cordierite-bearing micaschist towards the dome core (Thompson and Bard 1982; Fréville et al. 2016). Migmatitic orthogneisses (e.g. the Caroux

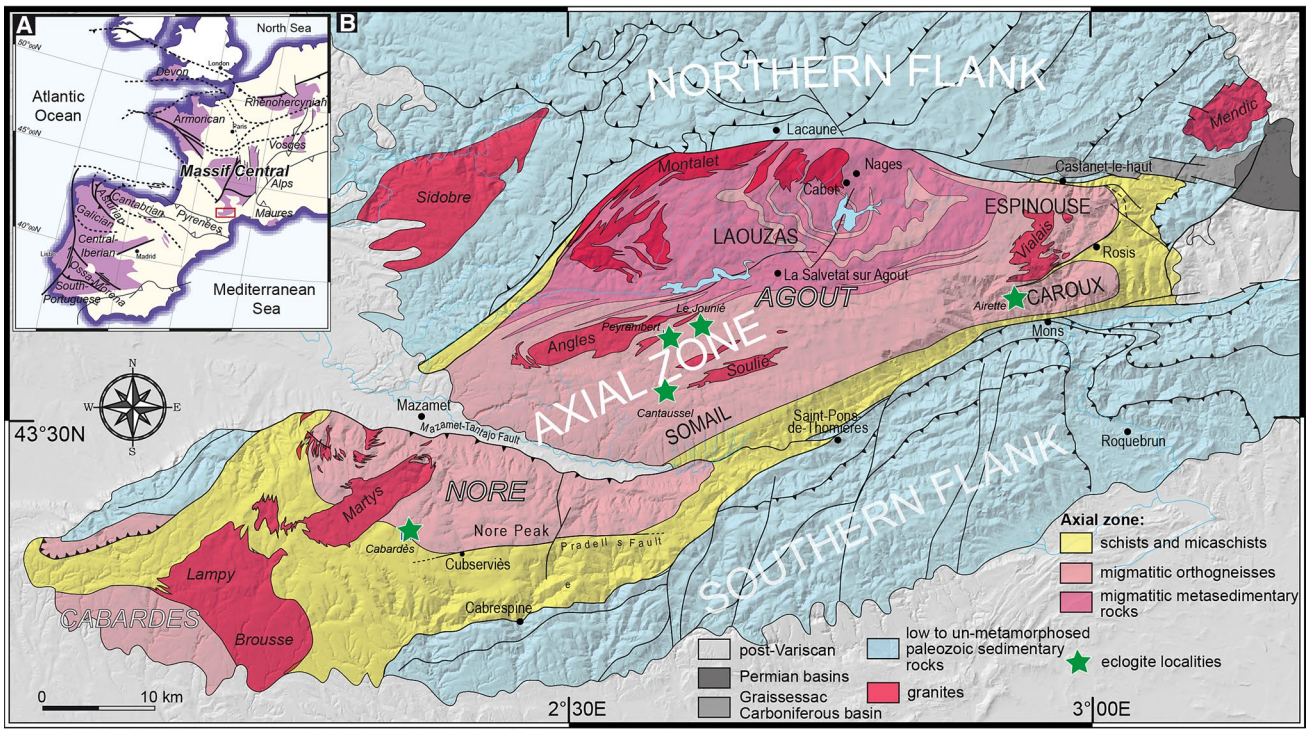

Fig. 1 **a** Location of the Montagne Noire massif within the western European Variscan belt (modified from Ballèvre et al. 2012). **b** Geological map of the Montagne Noire massif showing the three major domains: the northern flank, southern flank and the MNAZ in the middle

orthogneiss), make up the southern part of the MNAZ, from the eastern Caroux to the western Nore dome (Fig. 1). The protolith of the Caroux orthogneiss is an Ordovician granite that intruded within the sedimentary pile made of pelite, greywacke, quartzite, rare volcanics and carbonate (Alabouvette et al. 2003; Roger et al. 2004). These sediments presently crop out as metatexite within the deeper part of the dome, i.e. the Laouzas-Espinouse area (Fig. 1b). In the Laouzas-Espinouse area, the metapelitic metatexites are associated with leucocratic diatexites corresponding to heterogeneous cordierite-bearing Laouzas granitoids (Figs. 1, 2). The Vialais, Anglès, Soulié, Montalet and Martys granites (containing biotite ± muscovite ± garnet) are major plutonic intrusions of the MNAZ (Fig. 1b).

Structural setting

The MNAZ overall geometry is an elongate dome ~90 km long and ~20 km wide, with a sigmoidal shape in map view (Figs. 1b, 2a). The MNAZ is subdivided into two domes named the Agout and the Nore domes and separated by the Eocene north-directed reverse Mazamet Fault (Fig. 1b). Most of studies have focused on the Agout dome, which is composed of the northern Espinouse subdome and the southern Caroux subdome, with the Rosis synform located in between (Fig. 1b). Recently these three structures have been interpreted as a double dome with a high-strain zone that continues the Rosis synform towards the west in the core of the dome (Rey et al. 2011, 2012; Roger et al. 2015; Whitney et al. 2015). This interpretation and the tectonic model for the genesis of the Caroux/Espinouse is highly debated (Arthaud 1970; Echtler and Malavieille 1990; Matte et al. 1998; Aerden and Malavieille 1999; Demange 1998; Franke et al. 2011; Pitra et al. 2012; Van Den Driessche and Brun 1992; Van Den Driessche and Pitra 2012; Rey et al. 2011, 2012). The Caroux area is also interpreted as a large E–W trending antiform made of an early syn-thickening foliation subsequently folded during N-S-directed shortening and/or associated to an upward displacement of deeper crustal rocks (Faure and Cottereau 1988; Rey et al. 2011, 2012). Alternative models suggest that the Caroux massif is not a dome, but resulted from the upward bending of the footwall (the Caroux gneiss) of an extensional system controlled by a north dipping detachment fault (the Espinouse detachment) located along the northern flank of the Espinouse massif (Van Den Driessche and Brun 1992; Brun and Van Den Driessche 1994; Pitra et al. 2012; Van Den Driessche and Pitra 2012).

The recent study of Rabin et al. (2015) argues that the Caroux dome does not represent a unique foliation envelope folded into a N80° trending antiform but represents a complex heterogeneous structure made by the

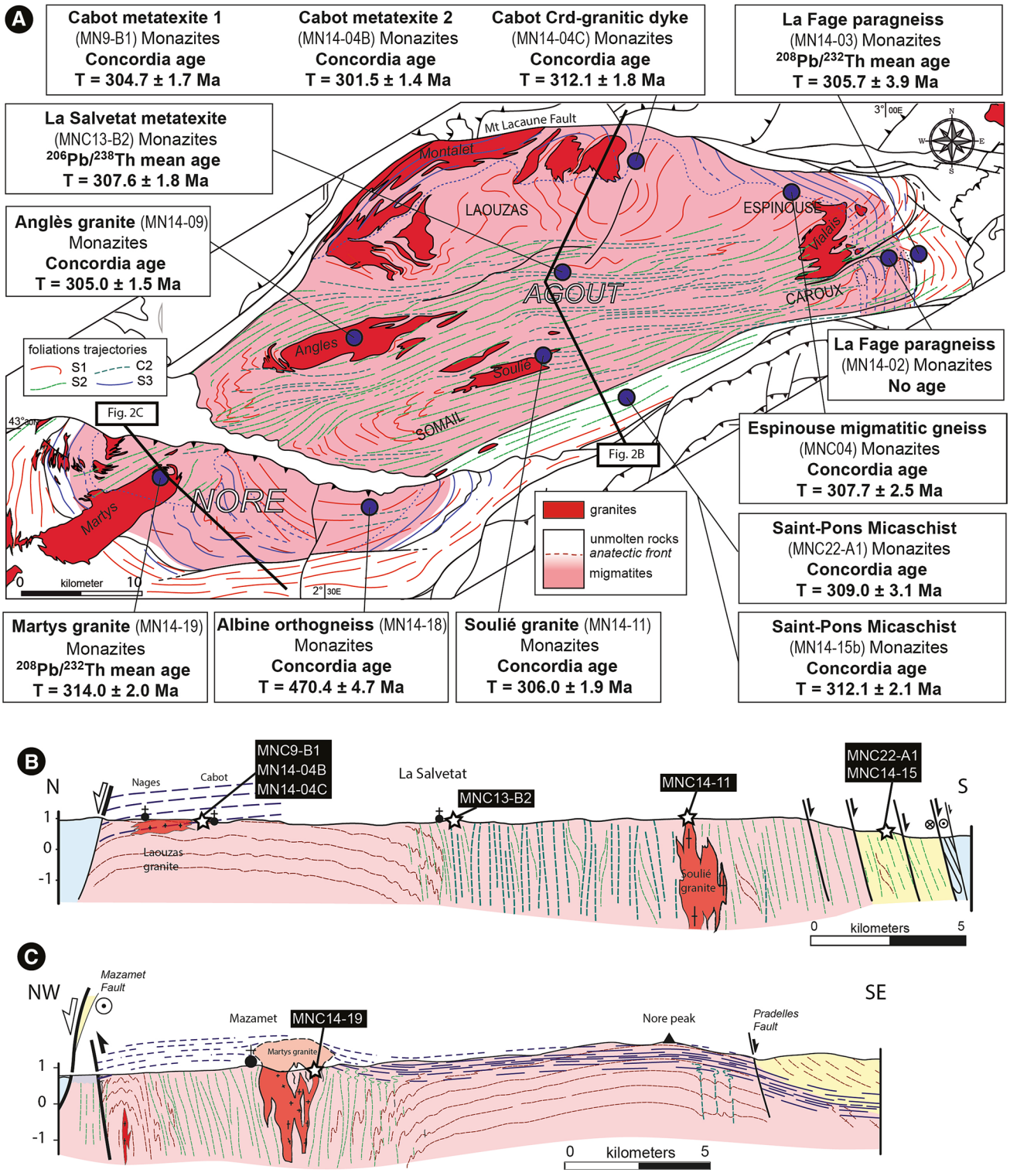

Fig. 2 **a** Structural map of the MNAZ showing S1, S2 and S3 foliation trajectories (modified from Rabin et al. 2015) with geochronological results and sample locations. **b**, **c** North–South trending cross sections through the MNAZ showing S1, S2 and S3 attitudes and relationships (modified from Rabin et al. 2015), and dated sample locations

superposition of at least three distinct planar fabrics S1, S2, and S3. These three planar fabrics are well represented at the scale of the whole MNAZ, and their geometry and location are shown in Fig. 2.

In this scheme, the early foliation S1 was originally flat lying in the core of the MNAZ and weakly dipping towards external zones in the dome envelope (Fig. 2a, b). S1 formed during crustal thickening that may have occurred after southward nappe stacking defined as the D1/M1 tectono-metamorphic event (e.g. Matte et al. 1998; Franke et al. 2011; Faure et al. 2014). However, strong deformation and metamorphism during D2 and D3 make it difficult to decipher the D1 kinematics.

The early flat-lying S1 was folded by D2 upright ENE–WSW folds and transposed in the central and southern part of the MNAZ into steep D2 high-strain zones (Fig. 2, Rabin et al. 2015). These are consistent with D2 NW–SE horizontal shortening, in a bulk contractional coaxial deformation regime that progressively evolved towards a non-coaxial dextral transpression. D2 was coeval with partial melting with metamorphic conditions that culminated at 0.65 ± 0.05 GPa and 720 ± 20 °C that correspond to the D2/M2 tectono-metamorphic event (Rabin et al. 2015; Fréville et al. 2016).

Along the anatectic front, S1 and S2 foliations were transposed into a flat-lying S3 foliation with top-to-NE or top-to-SW shearing in the NE and SW dome terminations, respectively. These structures define a D3 transition zone related to vertical shortening during coaxial thinning with a preferential NE–SW- to E–W-directed stretching. Depending on structural levels, the metamorphic conditions associated with D3/M3 event range from partial melting conditions in the dome core to subsolidus conditions above the D3 transition zone. Rabin et al. (2015) suggest that D2 and D3 deformation events are synchronous and resulted from strain partitioning on both sides of the anatectic front.

Metamorphic evolution

In the literature, two distinct metamorphic events are documented within the MNAZ. The earliest metamorphic event M1 corresponds to a medium to high-pressure (HP) event, characterized by the rare occurrence of kyanite-bearing micaschists and eclogite boudins within the migmatitic gneisses (see eclogite locations on Fig. 1) (Demange 1985; Soula et al. 2001; Alabouvette et al. 2003; Whitney et al. 2015). Demange (1985) estimated P–T conditions at 0.9 ± 0.2 GPa and 700 ± 50 and 800 ± 100 °C on the Carbardès and Le Jounié omphacite–garnet–quartz–rutile-bearing eclogite. Franke et al. (2011) obtained minimum peak conditions at >1.4 GPa and >650 °C that are in agreement with P–T results of ca. 1.4 GPa and 725 ± 25 °C from Whitney et al. (2015). The age of eclogite metamorphism in the Montagne Noire was previously thought to be ~430 Ma (U–Pb zircon lower intercept age, Gebauer and Grünenfelder 1982). Faure et al. (2014) determined a Sm–Nd isochron age of 358 ± 9 Ma for a Peyrambert eclogite boulder and they interpreted this age as the timing of the high-pressure metamorphism (M1). Whitney et al. (2015) obtained a zircon LA-ICP-MS U–Pb age at 315.3 ± 1.6 Ma interpreted to date the high-pressure conditions. For these authors, the age of the eclogite facies metamorphism at 315 Ma is synchronous with early stages of dome formation and granite/migmatite crystallization at 315–300 Ma (Roger et al. 2015).

The second metamorphic event M2 shows a low-pressure–high-temperature (LP–HT) metamorphic gradient of up to 50 °C/km that is defined by isograds wrapping around the gneiss core and tightening along the flanks of the dome (Bard and Rambeloson 1973; Ourzik et al. 1991; Demange 1996; Soula et al. 2001; Alabouvette et al. 2003; Fréville et al. 2016). The LP–HT metamorphism (M2) is accompanied by granitic magmatism and pervasive migmatization of the gneiss dome (Soula et al. 2001) as documented by P–T conditions of partial melting in the Laouzas migmatite that have been estimated at 0.45 GPa–620 °C by Ourzik et al. (1991).

Recently, Rabin et al. (2015) showed that partial melting may have started at the end of the prograde metamorphism (D1/M1 event) and was probably coeval with the onset of D2 deformation. Quartz–feldspar–biotite–sillimanite–garnet–cordierite-bearing migmatites recorded a clockwise evolution with peak temperatures and pressures around 750 ± 50 °C and 0.65 ± 0.05 GPa, respectively, followed by a decompression path with cooling down to 680 ± 50 °C at 0.4 ± 0.1 GPa. Fréville et al. (2016) suggest that migmatization of the Caroux orthogneiss, in the eastern MNAZ, occurs after fluid-present and muscovite breakdown reactions during prograde evolution with conditions at 680 ± 50 °C and 0.7–0.8 ± 0.1 GPa.

The Salvetat and Ourtigas migmatites have been dated at 327 ± 7 and 326 ± 4 Ma by the EPMA method (electron probe micro-analysis) on monazite by Faure et al. (2010). These authors suggest that the migmatization and emplacement of anatectic granitoids (Laouzas and Montalet) took place around 333–326 Ma and late granitoids (Anglès, Vialais, Soulié) emplaced around 325–318 Ma. Recently, Roger et al. (2015) suggested that the U–Th–Pb LA-ICP-MS or/and TIMS (Thermal Ionization Mass Spectrometry) monazite ages obtained from the Héric augen gneiss (308 ± 3 Ma), late kinematic Vialais granite (303 ± 4 Ma), and post-kinematic Ourtigas leucogranite (298 ± 2 Ma), bracket the high-temperature deformation and metamorphism at ~310–300 Ma, clearly post-dating regional contraction and nappe emplacement (>320 Ma; e.g. Franke et al. 2011). These young ages are similar to

the K–Ar (Franke et al. 2011; Doublier et al. 2014) and $^{40}Ar/^{39}Ar$ (Maluski et al. 1991) ages obtained on muscovite and biotite, both in the uppermost gneiss of the MNAZ and in Paleozoic southern and northern flanks.

Within the micaschists along the southern MNAZ envelope, Rabin et al. (2015) suggest a peak of metamorphism culminating at 0.65 ± 0.05 GPa and 630 ± 20 °C that was coeval with D2 deformation. Structural results suggest that D2/M2 and D3/M3 event were synchronous but spatially partitioned within the crust (Rabin et al. 2015).

Plutonism

Several late granitoids intruded the migmatites of the MNAZ and their emplacement age also is debated. Recently, the Vialais granite, in the eastern part of the Espinouse dome, was dated at 305–300 Ma using TIMS and LA-ICP-MS on monazite, zircon and xenotime grains (Roger et al. 2015) (Fig. 1). Previous studies reported ages between 330 and 320 Ma. Matte et al. (1998) reported TIMS zircon and monazite ages at 327 ± 5 Ma and Faure et al. (2010) reported EPMA monazite age at 320 ± 3 Ma. The duality about emplacement age of the granites (330–320 or 305–300 Ma) also exists for the Montalet granite and the anatectic Laouzas granite (Fig. 1). The Montalet granite, located along the north-western edge of the MNAZ, is a biotite and ± garnet-bearing peraluminous granite considered as an early plutonic body (Demange 1996; Alabouvette et al. 2003). U–Th–Pb EPMA analysis on monazite yielded an age at 327 ± 7 Ma for the garnet-rich facies and at 333 ± 4 Ma for the biotite-rich facies (Faure et al. 2010). Based on the data published by Faure et al. (2010), Roger et al. (2015) have recalculated a weighted average $^{206}Pb/^{238}U$ age of 305 ± 10 Ma for the Montalet granite. Poilvet et al. (2011) have shown that the Montalet granite is a syntectonic intrusion. They have analysed a sample of the garnet-rich facies, collected at the Picotalin pass near the Mont de Lacaune fault (Fig. 1b), that yielded U–Th–Pb LA-ICPMS ages of the 294 ± 1 (monazite) and 294 ± 3 Ma (zircon). They interpreted this age of 294 Ma as the emplacement age of the Montalet granite. Faure et al. (2010) also analysed the Laouzas cordierite granite, they obtained an EPMA monazite age of 333 ± 6 Ma and a SIMS (Secondary Ion Mass Spectrometry) zircon age of 299 ± 3 Ma.

The biotite-rich Anglès granite was dated by EPMA on monazite at 325 ± 7 Ma (Faure et al. 2010). The muscovite + biotite ± garnet Soulié granite yielded an EPMA monazite age at 318 ± 4 Ma (Faure et al. 2010). The Martys granite gave a Rb–Sr whole-rock isochron age at 300 ± 34 Ma (Hamet and Allegre 1976) (Fig. 1b). The end of magmatism was marked by several generations of late pegmatitic and undeformed granitic dikes that intruded the gneissic rocks of the MNAZ between 292.0 ± 4.4 Ma and 297.2 ± 5.3 (K–Ar muscovite) (Franke et al. 2011).

Analytical methods

U–Th–Pb geochronology of zircon, monazite and xenotime was conducted by LA-ICP-MS at the Laboratoire Magmas et Volcans, Clermont-Ferrand (France). Zircon and monazite grains were ablated with a Resonetics Resolution M-50 powered by an ultrashort-pulse ATL Atlex Excimer laser system at a wavelength of 193 nm (Müller et al. 2009). The detailed analytical procedures are described in Hurai et al. (2010) and Roger et al. (2012, 2015) and in the supplementary material (Table S1). Data reduction was carried out with the GLITTER® software package developed by Macquarie Research Ltd (Jackson et al. 2004). The decay constants used for the U–Th–Pb system are those determined by Jaffey et al. (1971) and recommended by IUGS (Steiger and Jäger 1977). Ages and diagrams were generated using the Isoplot/Ex v. 2.49 software package by Ludwig (2001). In the text, the tables and figures, all uncertainties in ages and isotopic ratios are given at $\pm 2\sigma$.

The discordant data analysed by the LA-ICP-MS method were considered only if they allowed possible discordia lines to be defined on the concordia diagrams; otherwise they were not taken into consideration because of doubtful interpretation. In laser ablation ICP-MS analyses, several factors that cannot be easily detected from the inspection of the time-resolved signals might contribute to discordance (e.g. common Pb by way of low U content inclusions, mixing of different age domains, small cracks). Monazite data obtained by LA-ICP-MS were plotted in a U–Th–Pb concordia diagram ($^{206}Pb/^{238}U$ vs $^{208}Pb/^{232}Th$) because ^{232}Th measurement is more accurate than ^{235}U.

U–Th–Pb results

In this section, we present new geochronological data for the three rock types, i.e. migmatitic metapelites, micaschists and granites (Table 1). For each sample, (1) the petrological features of rock-forming and accessory minerals are detailed with relationships between the fabrics and mineralogical assemblage investigated considering D1, D2 and D3 (Rabin et al. 2015) and (2) the geochronological results are presented. The field location of each sample is detailed on Fig. 2. Monazite and xenotime grains within the metamorphic rocks were analysed in situ in thin section in order to preserve textural relationships between these accessory minerals, the rock-forming mineralogical assemblage and the fabrics. Analysis of monazite, xenotime and

Table 1 Summary of the geographic position, rock type and geochronological data for the samples analysed in this study

Sample	Rock type	Location	U–Th–Pb age (±2σ)	Peak T metamorphic conditions	Fabrics
MN14-18	Albine orthogneiss	N43°26.562′	472.1 ± 2.8 Ma (Z)		Weak S2 foliation
		E02°31.677′	470.4 ± 4.7 Ma		
MN14-11	Soulié granite	N43°32.612′ E02°37.607′	306.0 ± 1.9 Ma		
MN14-09	Anglès granite	N43°33.968′ E02°33.234′	305.0 ± 1.5 Ma		
MN14-19	Martys granite	N43°28.415′ E02°22.177′	314.0 ± 2.0 Ma		
MN14-04C	Cabot Crd–granite	N43°39.968′ E02°46.257′	312.1 ± 1.8 Ma		
MN14-04B	Cabot metatexite	Idem	301.5 ± 1.4 Ma (T.S.)		S1–S3 foliation
MN9-B1	Cabot metatexite	Idem	304.7 ± 1.7 Ma (T.S.)		S1–S3 foliation
MNC04	Espinouse metatexite	N43°44.149′ E03°09.000′	307.7 ± 2.5 Ma (T.S.)	4.3 ± 1 kbar; 705 ± 45 °C	S3 foliation
MN14-03	La Fage fine-grained gneiss	N43°36.309′	305.7 ± 3.9 Ma		S3 foliation
		E03°00.540′	284 ± 13 Ma (T.S.)		
MN13-B2	La Salvetat metatexite	N43°36.086′	307.6 ± 1.8 Ma	6.2 ± 0.7 kbar; 725 ± 20 °C (peak T conditions)	S1–S2 foliation
		E02°42.359′	(T.S.)	4.4 ± 0.5 kbar; 685 ± 25 °C (retrograde conditions)	
MN22-A1	Saint Pons micaschist	N43°30.807′ E02°44.395′	309.0 ± 3.1 Ma (T.S.)	6.5 ± 0.5 kbar; 630 ± 20 °C	S1–S2 foliation
MN14-15b	Saint Pons micaschist	N43°30.795′ E02°44.403′	312.1 ± 2.1 Ma (T.S.)	6.5 ± 0.5 kbar; 630 ± 20 °C	S1–S2 foliation
MN14-02	La Fage metatexite	N43°36.550′ E03°00.531′	No age (T.S)		S3 foliation

The location of the various data is plotted by blue circles on Fig. 2a. *T.S.* thin section, *Z* zircon

zircon from magmatic rocks where textural relations were not required, was performed using laser ablation ICP-MS on separated crystals.

Migmatites within the MNAZ dome core

Cabot migmatites

Two metatexites were sampled along the D62 road east of the Cabot village (sample MN9B1 and MN14-04B, Fig. 2, Table 1). At outcrop scale, the migmatitic foliation dips weakly towards the east. It corresponds to a S1–3 foliation (Fig. 3a). Within the MNAZ structural framework, the Cabot migmatites lie along the D3 transition zone (Fig. 2b). In this area, when S1 and S3 are distinguished, as observed near Cabot and Nages, S1 is folded with S3 that parallels the axial plane of F3 folds (Fig. 3b).

The Cabot migmatite, sample MN9-B1, consists of a medium-grained quartz–K feldspar–plagioclase–biotite–cordierite assemblage. Cordierite appears as 250-µm- to 1–2-mm-large porphyroblasts locally retrogressed into chlorite and clays. The preferential alignment of biotite and elongated quartz aggregates defines a composite S1–S3 foliation with similar mineral assemblages for S1 and S3 fabrics (Fig. 3c). In this sample, all monazite grains are included in biotite except Mz3 (Table S2), which is located at the boundary between a biotite crystal and the quartzo-feldspathic matrix. Thirteen analyses obtained on seven monazite grains included in a biotite crystal and one analysis on a matrix monazite were performed. All these data have a concordant to subconcordant position (96–100% of concordance). They form a cluster around 295 to 310 Ma and yield a concordia age of 304.7 ± 1.7 Ma (MSWD = 1.4; $N = 13$) (Table S2; Fig. 4a).

The Cabot migmatite, sample MN14-04B, is a medium-grained quartz–K feldspar–plagioclase–biotite ± garnet-bearing migmatitic metapelite. Garnet is rare and 100 µm in size. Leucocratic quartz–feldspar mm-sized pockets are considered as crystallized granitic melt (leucosome). Two planar fabrics that correspond to S1 and S3 are depicted.

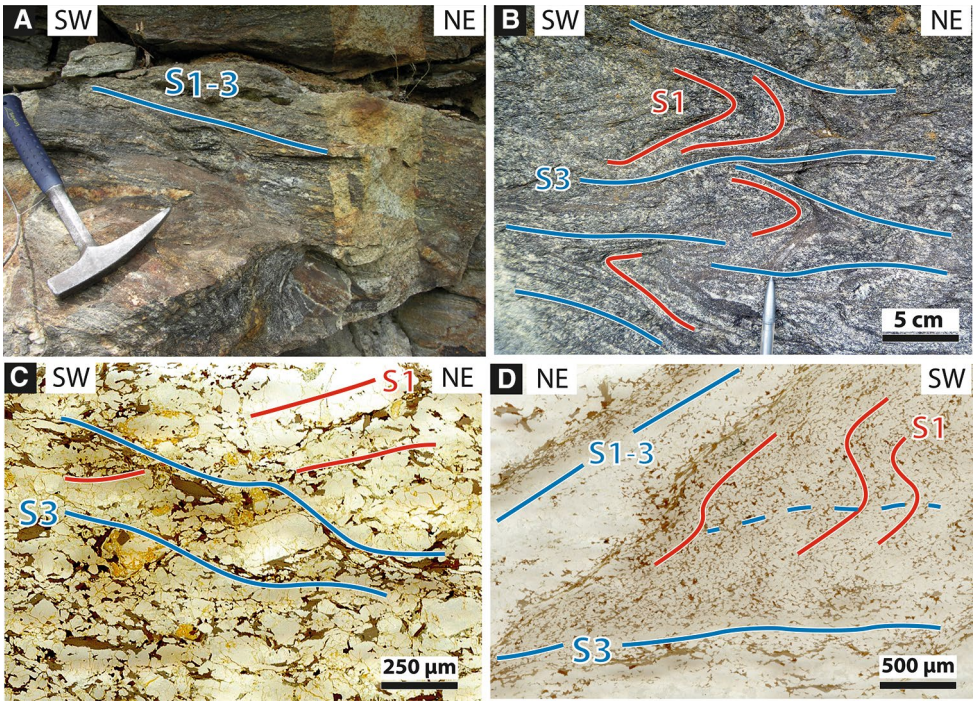

Fig. 3 Field photographs and microphotographs of Cabot migmatitic rocks [see location on Fig. 2, (WGS 84: 43.67270°N; 2.77647°E)]. **a** Cabot metatexite with a flat-lying S1–3 foliation cross-cut by a cordierite-bearing leucocratic dyke (sample MN14-04C). **b** Cabot metatexite showing D3 folding of S1 and the development of flat-lying S3 foliation. **c** Microphotograph of the Cabot metapelite sample MN9-B1 showing the medium-grained quartz–K feldspar–plagioclase–biotite–cordierite assemblage with 250 µm-large cordierite grains retrogressed into chlorite and clays. **d** Microphotograph of the cabot metapelite sample MN14-04-B showing a fine to medium-grained quartz + K feldspar + plagioclase + biotite ± garnet-bearing assemblage with leucocratic quartz + feldspar mm-size pockets representing leucosome. S1 is folded together with the development of S3

S1 is folded together with the development of S3 (Fig. 3d). There are two textural occurrences of monazite grains (isolated or cluster) in sample MN14-04B (Table S2). Twenty-four analyses were carried out on three isolated monazite grains and on 21 monazites belonging to six clusters (Table S2, Fig. 4b). All grains are included in biotite except a cluster Mz-A3 (spot 11, 12 and 13), which is located in the matrix. In the concordia diagram, all data plot in concordant to subconcordant position (96–103% of concordance), 22 points plot around 300 Ma, one at ~320 Ma (spot 16) and one at ~350 Ma (spot 1) (Table S2, Fig. 4d). These two analyses (spot 1 and 16), which present older ages could be either (1) a mixture between an older monazite domain (probably Ordovician) and a variscan domain or (2) represent an inherited component. The 22 other data yield a concordia age of 301.5 ± 1.4 Ma (MSWD = 0.97; $N = 22$).

The Cabot cordierite-bearing granite dyke

The Cabot cordierite-bearing dyke (MN14-04C) is a near-vertical 25-cm-thick dyke that intrudes the Cabot flat-lying stromatic migmatites (MN14-04B) (Fig. 3a). It is a leucocratic granite with large K feldspar separated by fine-grained quartz. Large cordierite (1–2 mm) with sillimanite inclusion is associated with biotite as rounded aggregates. Myrmekite and few tourmalines are present. Monazite and xenotime crystals are mainly euhedral, of moderate size (100–200 µm), greenish and transparent. All analysed xenotime grains have similar low Th/U ratios (0.1) with medium Pb (324–1222 ppm) and Th (511–2801 ppm) contents, and medium–high U content (9053–30,445 ppm). While monazite grains have more heterogeneous contents: medium Pb (324–1222 ppm) concentration, high U content (7566–19,524 ppm) and very high Th concentration (34,671–89,433 ppm) (Table S3). The Th/U ratios are variable between 2.5 and 9.3.

Thirteen spots on nine monazite grains were performed (Table S3). All data are concordant (100–103% of concordance). Except two analyses (spot 14 and 15) obtained on one monazite grain (Mz4; which is younger with a $^{208}Pb/^{232}Th$ mean age = 294.4 ± 3.4 Ma), all monazite data form a cluster around 310–315 Ma and the concordia age is 312.1 ± 1.8 Ma (MSWD = 0.67; $N = 11$) (Fig. 4c). Nine xenotime crystals from this sample were also analysed (13 spots in total). On a concordia plot, except spot 9 (93% of

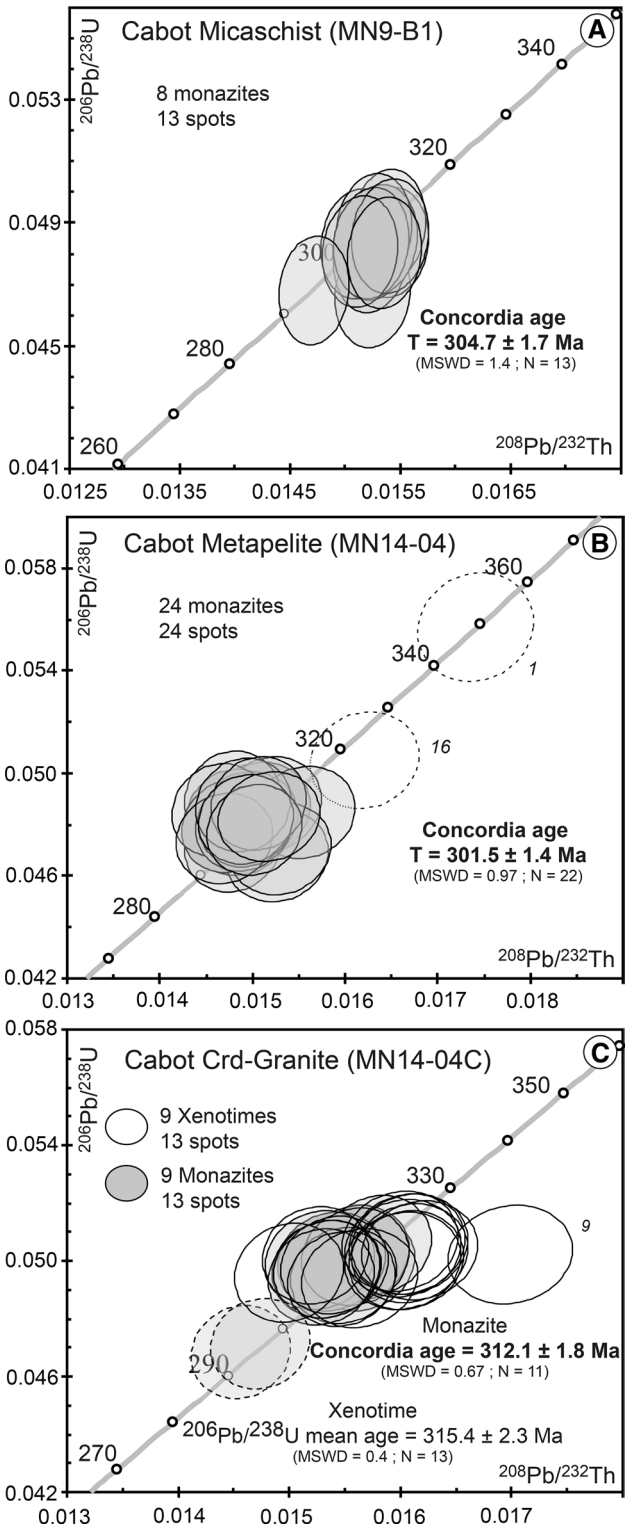

Fig. 4 Monazite and xenotime U–Th–Pb Concordia diagrams for three samples collected near Cabot Village. *Error ellipses* and uncertainties in ages are $\pm 2\sigma$. The *stippled ellipses* are not taken into account for the age calculation and the numbers refer to analytical data in Table S2 or 3. **a** Cabot Metatexite (MN9-B1); **b** Cabot metatexite (MN14-04B) and **c** Cabot cordierite-bearing dyke (MN14-04C)

the concordance), 12 analyses are concordant to subconcordant (98–104% of concordance) and have similar positions with the monazite data. However, a slight discrepancy may be related to a matrix mismatch due to the use of a monazite standard. The weighted average $^{208}Pb/^{232}Th$ age for these data is 315.4 ± 2.3 Ma (MSWD = 0.3; $N = 13$) (Fig. 4c), in agreement with the concordia age obtained on the monazite grains. All weighted average ages are similar in the error bars. The best age estimate is provided by the concordia age of 312.1 ± 1.8 Ma.

Espinouse metatexite

Sample MNC04 was collected within the S3 transition zone (Fig. 2, Table 1). It is a migmatitic gneiss that is composed of biotite, sillimanite, cordierite, quartz, plagioclase and K feldspar with rare muscovite. Biotite and muscovite grains, homogeneous in composition, form the main S3 foliation and are considered to belong to the peak equilibrium assemblage (Fig. 5a; Fréville et al. 2016). Locally, sillimanite and cordierite are arranged as centimetric nodules that parallel S3 and L3. This suprasolidus mineralogical assemblage records peak temperature conditions at 705 ± 45 °C and 0.43 ± 0.1 GPa (Fréville et al. 2016). Accessory minerals (monazite, xenotime) present various textural positions. They can be included in biotite porphyroblasts (Xe1, Mz3) or in biotite–sillimanite aggregates (Mz6, Mz7). Grains are also present in the quartzo-feldspathic matrix (Mz5, Mz8) and can be located close to a biotite grain boundary (Mz2, Mz4) (Table S2).

Four analyses obtained on one xenotime grain included in a biotite crystal and 16 analyses on 14 monazites were performed. There is no age difference between the included grains and the matrix monazite (Table S2). Age scattering corresponds to variation from one crystal to another as well as heterogeneities within single crystals. Except for spot 6 (75% of the concordance) obtained on a monazite included within a biotite, all the data form a cluster around 300–320 Ma and yield a $^{206}Pb/^{238}U$ mean age of 308.3 ± 2.4 Ma (MSWD = 1.2; $N = 19$) (Table S2, Fig. 6a). Thirteen data are concordant to subcorcordant (except spots 3, 6, 9, 15, 16, 17, 19), the $^{206}Pb/^{238}U$ mean age is 307.7 ± 2.5 Ma (MSWD = 1.07; $N = 13$), and the weighted average $^{208}Pb/^{232}Th$ age is 312.7 ± 3.1 Ma (MWSD = 3; $N = 13$), these ages are similar within error. The $^{206}Pb/^{238}$ U mean age is 307.7 ± 2.5 Ma and is interpreted as the best age estimation for the metamorphic event.

La Salvetat migmatite

Sample MN13-B2 consists in a medium-grained, quartz–K feldspar–plagioclase–biotite–sillimanite matrix with cordierite coronas surrounding garnet porphyroblasts

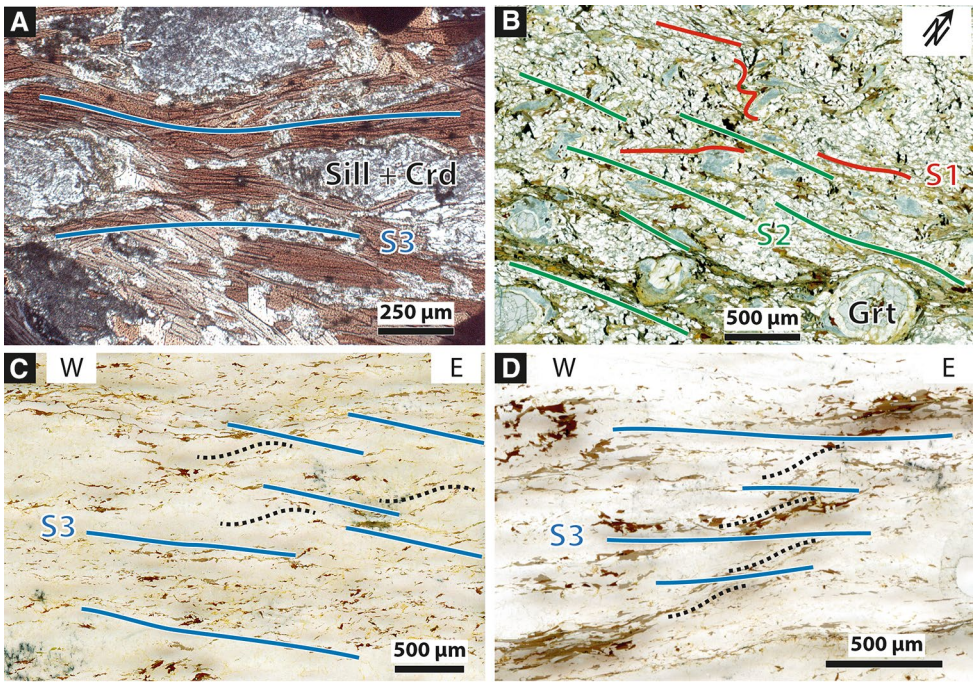

Fig. 5 **a** Microphotograph of MNCO4 migmatitic gneiss showing the sill + cd + biotite assemblage that marks S3 foliation. **b** Microphotograph of MN13-B2 La Salvetat metatexite with coronitic cordierite around garnet porhyroblasts. The main planar fabric is the subvertical ENE-trending S2 foliation. **c** Microphotograph of the MN14-02 La Fage migmatitic orthogneiss showing a strong S3 planar fabrics that dips weakly towards the east. **d** Microphotograph of the MN14-03 La Fage fine-grained gneiss with a quartz + feldspar + biotite + muscovite assemblage. Foliation S3 is defined by the preferential alignment of micas that dips weakly towards the east

(Fig. 5b). Cordierite is frequently associated with sillimanite and biotite. Preferential alignment of biotite and cordierite/sillimanite nodules defines two planar fabrics. An early foliation attributed to S1 is folded in response to horizontal shortening during D2. S2 develops as near axial planar vertical schistosity. There is no difference in mineralogical assemblage between S1 and S2 fabrics. In particular, biotite crystals within both S1 and S2 show similar chemical compositions (Rabin et al. 2015). The abundance of biotite and absence of muscovite suggest that melting occurred due to muscovite breakdown. Garnet porphyroblasts are not peritectic but inherited from amphibolite facies prograde metamorphism (Rabin et al. 2015). Pseudosection calculation indicates that this sample recorded peak metamorphic conditions at 0.62 ± 0.07 GPa and 725 ± 20 °C and retrograde conditions at 0.44 ± 0.05 GPa and 685 ± 25 °C corresponding to the cordierite-bearing assemblage (Rabin et al. 2015).

Monazite and xenotime are observed as inclusions in biotite–sillimanite fine-grained aggregates (Xe1-2, Mz1-5, Mz7-8, Mz10-11), biotite (Xe3, Mz9, Mz12) or cordierite porphyroblasts (Mz13-16, Xe5). Rare grains are located in the quartzo-feldspathic matrix (Xe4, Mz6; Table S2). Thirty-one spots on five xenotime grains (8 spots) and 16 monazite grains (23 spots) were analysed (Table S2). Except for spot 5, the $^{206}Pb/^{238}U$ ages range between 317.1 ± 9.3 and 294.1 ± 8.6 Ma with a weighted mean age of 308.4 ± 1.6 Ma (MSWD = 1.07; $N = 30$; Fig. 6b). Age scattering corresponds to variations from one crystal to another as well as heterogeneities within single crystals. There is no difference in age between included and matrix monazite. Without the more ±5% discordant data, the $^{206}Pb/^{238}U$ mean age is 307.6 ± 1.8 Ma (MSWD = 0.87; $N = 24$) and the $^{208}Pb/^{232}Th$ mean age is 306.3 ± 2.2 Ma (MWSD = 2.9; $N = 22$). The $^{206}Pb/^{238}U$ mean age is 307.6 ± 1.8 Ma and is interpreted as the best estimation of the metamorphic age.

La Fage metatexite

La Fage metatexite MN14-02 is a migmatitic Caroux orthogneiss that shows a strong S3 foliation (Fig. 5c). The rock is mainly quartzo-feldspathic with a low proportion of biotite. Monazite grains can be either included in muscovite (Mz2) or biotite (Mz4) or present in the quartzo-feldspathic matrix (Mz6, Mz7) (Table S2).

Nine spots on four monazites were performed (Table S2). In a concordia diagram, the ages are concordant (98–103% of concordance), but the ellipses are located between ~300 and 375 Ma. The $^{208}Pb/^{232}Th$ and $^{206}Pb/^{238}U$ ages are heterogeneous and are ranging from 298 ± 9 to 373 ± 11 Ma and from 303 ± 6 to 375 ± 8 Ma, respectively. This corresponds to variations from grain to grain as well as heterogeneities within grains. These data could reflect a mixture between a monazite domain older than 373 ± 11 Ma and a domain younger than 298 ± 9 Ma (Fig. 6c).

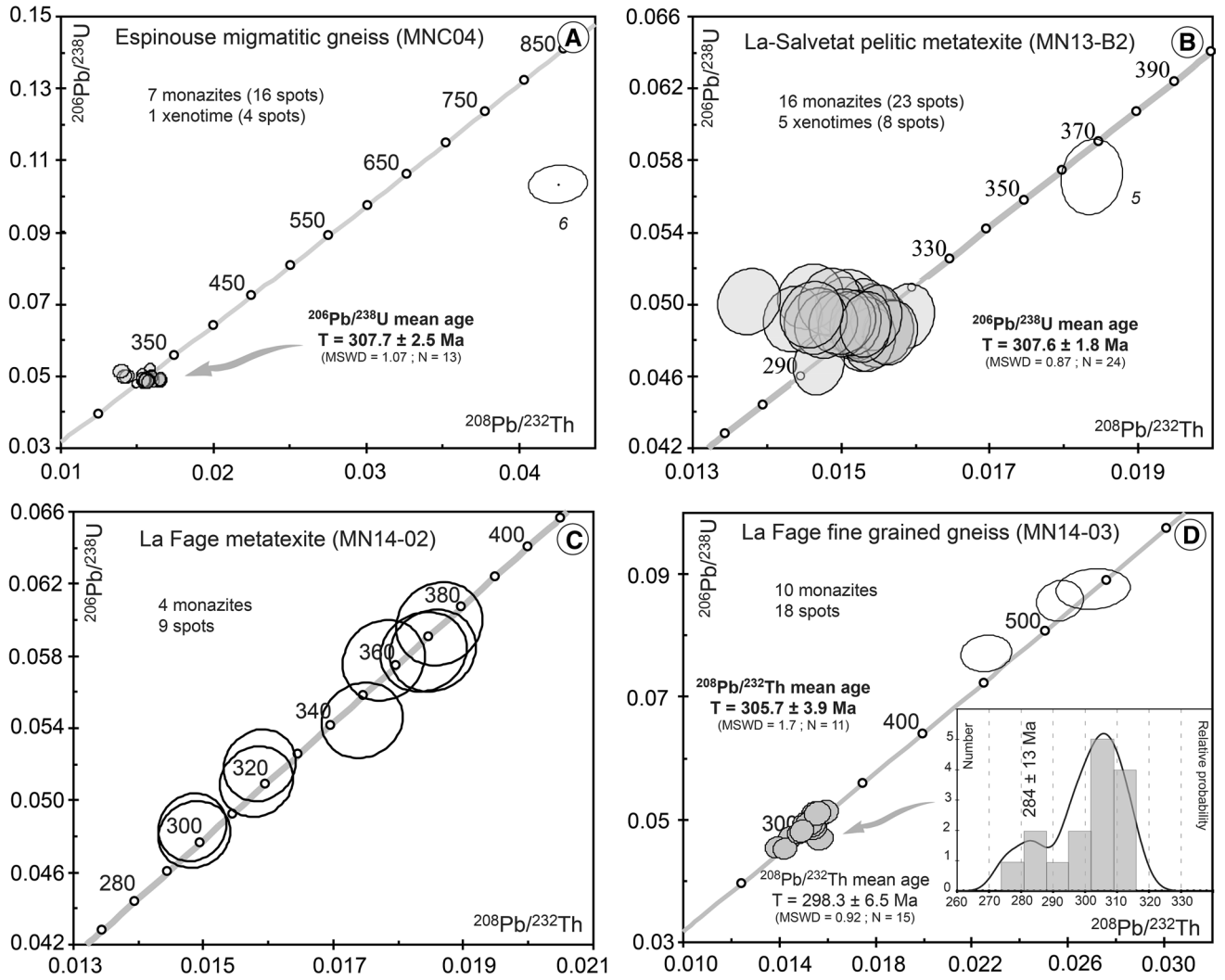

Fig. 6 Monazite and xenotime U–Th–Pb Concordia diagrams for migmatitic gneisses. *Error ellipses* and uncertainties in ages are $\pm 2\sigma$. The *white ellipses* are not taken into account for the age calculation and the numbers refer to analytical data in Table S2. **a** Espinouse migmatitic gneiss (MNC04); **b** La Salvetat migmatite (MN13-B2); **c** La Fage fine-grained gneiss (MN14-02). **d** The La Fage fine-grained gneiss (MN14-03)

Paragneiss and micaschists from the metasedimentary envelope

La Fage paragneiss (sample MN14-03)

The La Fage paragneiss, sample MN14-03, is a fine-grained gneiss with a quartz–plagioclase–K feldspar–biotite–muscovite assemblage. Foliation S3 is defined by the preferential alignment of micas that dips weakly towards the east (Fig. 5d). The monazite grains are included in biotite or muscovite porphyroblasts (Mz3, Mz5, Mz7-9, Mz13-14) or in the quartzo-feldspathic matrix (Mz6, Mz11-12). Eighteen spots on 10 monazites were performed, plotted in a concordia diagram, and the ellipses are concordant (94–106% of concordance) (Table S2, Fig. 6d). The heterogeneous $^{208}Pb/^{232}Th$ ages range from 275 ± 8 to 540 ± 26 Ma and correspond to variations between grains as well as heterogeneities within single crystals. Spots 1, 2 and 3 show very low Pb (9–26 ppm), Th (10–57 ppm) and U (135–432 ppm) contents and yield the oldest age at 540 ± 26, 512 ± 16 and 451 ± 17 Ma, respectively. These three data probably contain a Paleozoic inherited component. The probability histogram of concordant $^{208}Pb/^{232}Th$ vs $^{206}Pb/^{238}U$ ages for the 15 other analyses shows the presence of probably two different types of monazite grains related to two growth episodes. The minor population, four analyses (spots 4–7), is obtained on a matrix monazite (Mz6) and on monazite included in a biotite crystal (Mz5). Its $^{208}Pb/^{232}Th$ mean age is 284 ± 13 Ma (MWSD = 3.9; $N = 4$). While the main

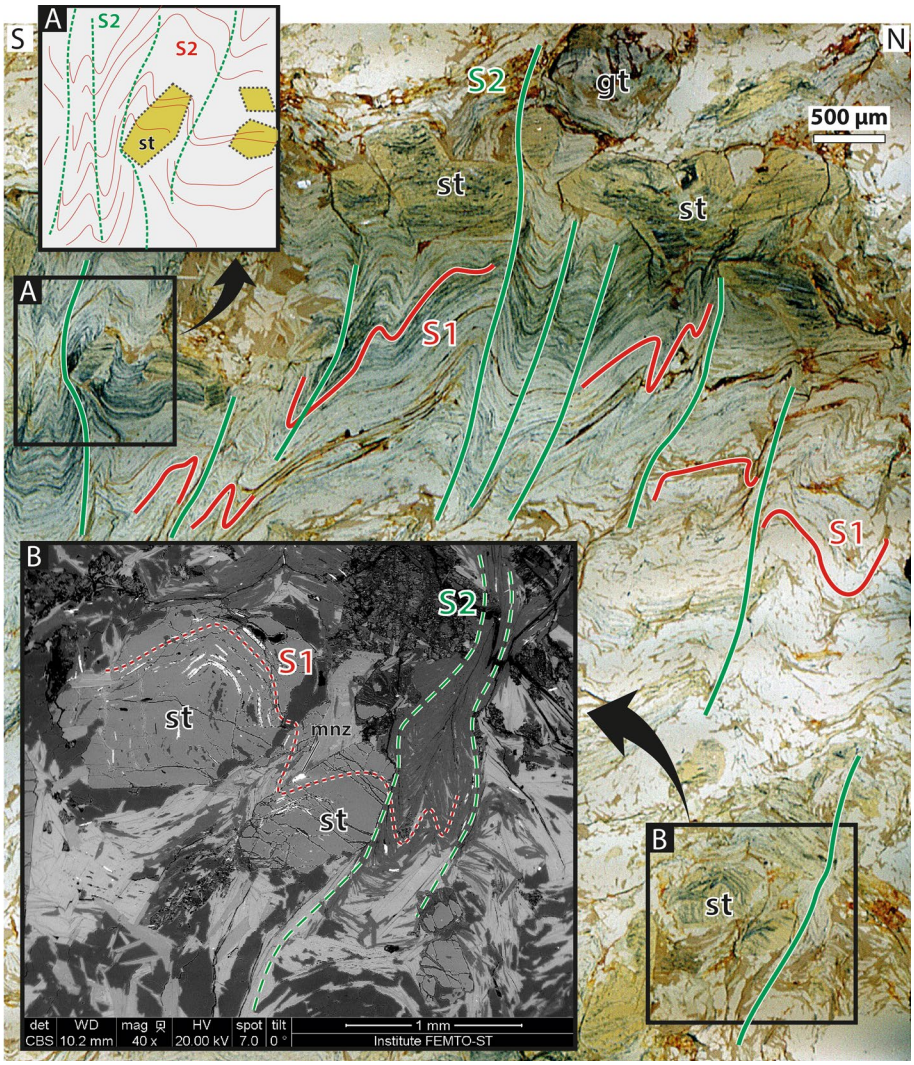

Fig. 7 Photomicrograph and scanning electron microscope (SEM) image from the Saint-Pons-de-Thomières micaschist (Sample MN1415b) showing the relationships between garnet–staurolite-bearing assemblage, S1 and S2. The subvertical S2 foliation is a partly transposed crenulation cleavage that deforms S1 with open-to-tight D2 folds. *Inserts a* and *b* The millimetre-scale staurolite porphyroblasts show the open-to-tight D2 folds as inclusions that argue for post-tectonic relation with S1. In addition, the external S2 foliation is slightly deflected and flattened around the staurolite porphyroblasts. Theses textural features indicate that staurolite grew during the onset on D2

population (matrix or inclusion) yields a $^{208}Pb/^{232}Th$ mean age of 305.7 ± 3.9 Ma (MWSD = 1.7; $N = 11$) (Fig. 6d), no correlation was found between U–Th–Pb ages obtained and grain textural position.

Saint-Pons-de-Thomières staurolite-bearing micaschists

The Saint-Pons-de-Thomières micaschists ("Saint Pons micaschist" and "St Pons micaschist" are interchangeable), samples MN14-15b and MN22-A1, are garnet–staurolite-bearing micaschists that were sampled at the same location, i.e. within the metasedimentary cover, north of the Saint-Pons-de-Thomières village (Fig. 2, Table 1). Both rocks show the same equilibrium quartz–plagioclase–biotite–muscovite–garnet–staurolite assemblage. The planar fabric S1–2 is steeply dipping towards the south and bears a subhorizontal crenulation lineation (Rabin et al. 2015). At millimetre scale, S1 is defined by the preferential alignment of micas. The foliation S1 is folded by D2 with the development of open-to-tight millimetre-to-submillimetre D2 folds and a related S2 crenulation cleavage that dips moderately to strongly towards the south (Fig. 7). Garnet porphyroblasts are 1–3 mm in size, euhedral to subhedral and show a Mn-rich core and a Mn-poor rim (Rabin et al. 2015). Subhedral staurolite crystals (0.2–5 mm) are homogeneous in composition irrespective of their textural position (Rabin et al. 2015). The staurolite porphyroblasts contain open-to-tight D2 folds defined by inclusion trails arguing for post-tectonic relation with S1. In addition, the external S2 foliation is somewhat deflected and flattened around the staurolite porphyroblasts (Fig. 7). Theses textural features indicate that staurolite grew during the onset of D2. The P–T conditions corresponding to the equilibrium assemblage biotite + plagioclase + quartz + muscovite + garnet + staurolite are 0.65 ± 0.05 GPa and 630 ± 20 °C representing peak temperature metamorphism (Rabin et al. 2015).

For the Saint-Pons-de-Thomières micaschist MN14-15b, most monazite grains are elongated with a shape ratio

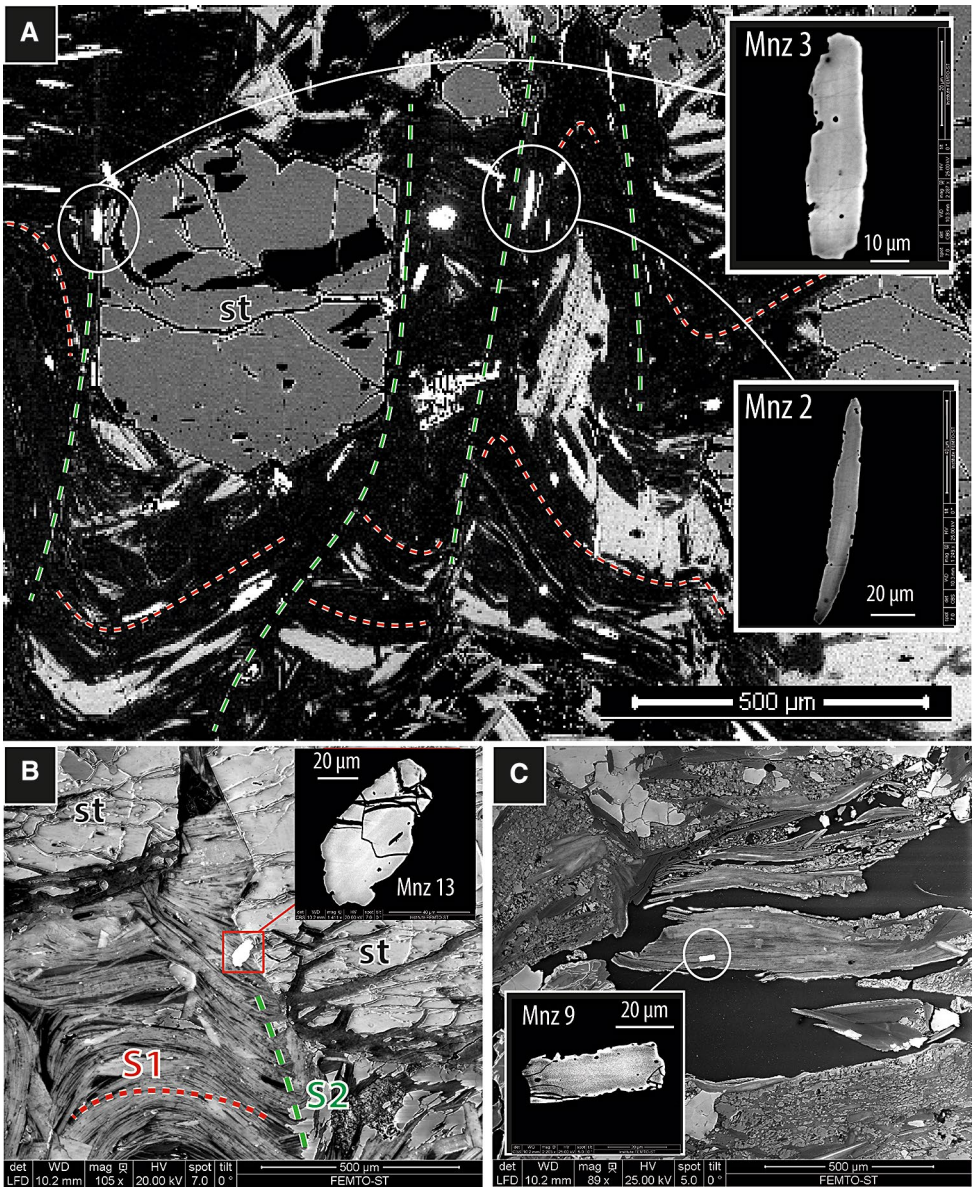

Fig. 8 SEM images showing the textural position of monazite grains within the Saint-Pons-de-Thomières Micashist. **a**, **b** Examples of monazite located along S2 with elongated grains that parallel S2 direction. **c** Example of monazite grains that parallel S1 foliation

up to 9 (Mz 2, Fig. 8a). Within the S1/S2 framework, Mz2, Mz3, Mz12, Mz5 and Mz13 are located along S2 with most of these grains elongated and parallel to the S2 direction (Fig. 8a, b). Some monazite grains are parallels to S1 (Mz4, Mz9, Mz10 and Mz11, Fig. 8c). Twenty-two spots on 10 monazites were analysed (Table S2). In a concordia diagram, the ages are concordant (100–106% of concordance) but the heterogeneous $^{208}Pb/^{232}Th$ ages, ranging from 302 ± 9 to 491 ± 14 Ma (spot 8), correspond to grain to grain variations or heterogeneities within crystals. Among these 22 analyses, eleven data form a cluster around 300–320 Ma (Table S2, Fig. 9a) and yield a $^{206}Pb/^{238}U$ mean age of 315.5 ± 2.9 Ma (MWSD = 1.8; $N = 11$) and a weighted average $^{208}Pb/^{232}Th$ age of 309.1 ± 2.6 Ma (MSWD = 0.92; $N = 11$). These ages are in agreement with the Concordia age of 312.1 ± 2.1 Ma (MSWD = 1.3; $N = 11$) obtained on these eleven data regardless of the textural position of the grains (Table S2). Among the eleven data that are not taken into account for the age calculation, ten ellipses (except spot 8) form a cluster around 360 Ma with a strong scattering of data between ~335 and ~390 Ma. The $^{206}Pb/^{238}U$ mean age is 364 ± 10 Ma (MSWD = 14; $N = 10$) and the $^{208}Pb/^{232}Th$ mean age is 359 ± 11 Ma (MWSD = 7.5; $N = 10$). The high MSWD (7.5 and 10) values imply that these two weighted averages cannot be interpreted as geologically meaningful ages. The 11 data most probably reflect a mixture between a monazite domain older than ca. 490 Ma and the younger variscan

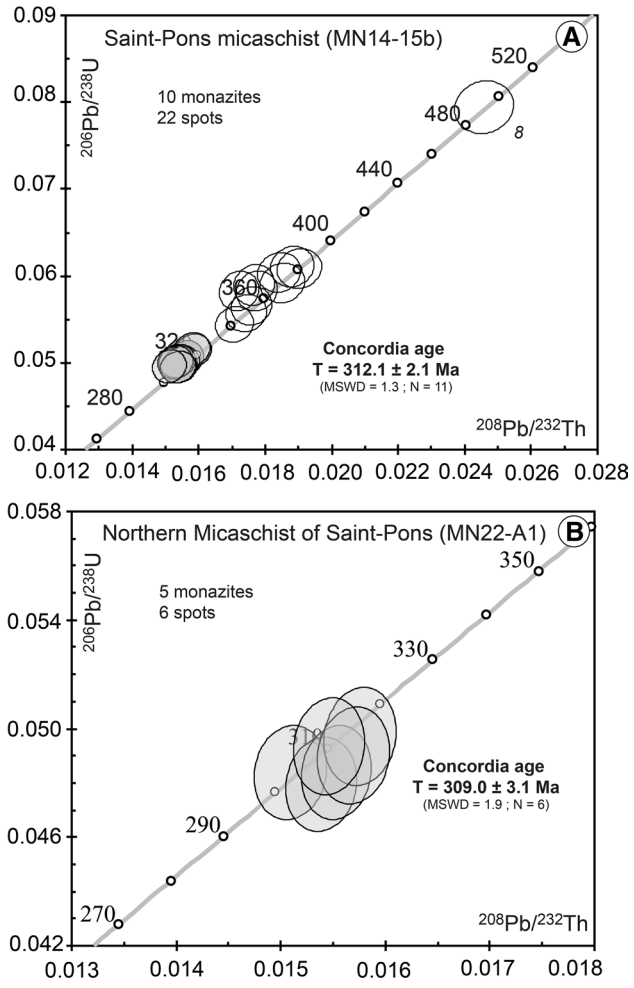

Fig. 9 Monazite U–Th–Pb Concordia diagrams for the Saint-Pons-de-Thomières micaschists **a** sample MN14-15b and **b** sample MN22-A1. See Fig. 2 for sample location. The *white ellipses* are not taken into account for the age calculation and the numbers refer to analytical data in Table S2. *Error ellipses* and uncertainties in ages are $\pm 2\sigma$

domain (Fig. 9a). The best age estimate is provided by the concordia age of 312.1 ± 2.1 Ma.

For the Saint-Pons-de-Thomières micaschist MN22-A1 (Fig. 9b), most monazite grains are included in biotite except Mz1 and Mz6, which are elongated in the S1–2 foliation. Six spots, obtained on four monazite grains included in biotite crystals and one analysis on one matrix monazite, were performed. All these data have a concordant to subconcordant position (98–101% of concordance), form a cluster around 300 to 315 Ma and yield a concordia age of 309.0 ± 3.1 Ma (MSWD = 1.9; $N = 6$), in agreement with the $^{206}Pb/^{238}U$ mean age of 306.8 ± 3.5 Ma (MWSD = 0.87; $N = 6$) and $^{208}Pb/^{232}Th$ mean age of 309.6 ± 5.5 Ma (MWSD = 3.3; $N = 6$) (Table S2; Fig. 9b). The best age estimate is provided by the concordia age of 309.0 ± 3.1 Ma.

Syn-kinematic granites

Three granites were studied, namely the Anglès (MN14-09), Soulié (MN14-11) and Martys (MN14-19) granites (Fig. 2, Table 1). These three granites are elongated bodies that parallel the ENE–WSW S2 trend and are intrusive within the migmatitic gneiss (Fig. 2). Weak solid-state D2 deformation microstructures with a vertical foliation are observed locally, mainly along granite boundaries. This is observed for example near the hamlet "Les Sires" where the Anglès granite shows a clear subvertical S2 foliation that trends N60. These granites show mainly a coarse grained texture with unclear magmatic anisotropy. However, based on petrofabric and ASM studies, Charles et al. (2009) show that the Anglès and Soulié granites have a subvertical magnetic foliation and a subhorizontal magnetic lineation consistent with other granitic-migmatitic rocks from the middle and southern part of the MNAZ. Considering these magmatic and solid-state features, we consider the Anglès and Soulié granites as syn-tectonic granites that emplaced during D2. The Martys granite intrudes the migmatitic gneisses along the steep S2 and the flat-lying S3 (Fig. 2, Rabin et al. 2015). There are no available ASM data on this granite, but geometrical relations between the Martys granite and the S2–S3 may suggest a late D2–D3 emplacement (Rabin et al. 2015). In these three granites, monazite and xenotime crystals are of moderate size (100–200 µm), yellow, transparent and the majority of grains exhibits euhedral and prismatic outlines. Concentric zoning in BSE is rare. It is usually indicative of a magmatic origin (Ayers et al. 1999; Williams et al. 2007). All analysed xenotime grains have uniformly low Th/U ratios (0.04–0.2) with medium Pb (339–620 ppm) and Th (685–2264 ppm) contents and medium–high U content (8871–14,555 ppm). Monazite grains show medium Pb content (437–1679 ppm), medium–high U content (953–11,688 ppm) and high to very high Th concentration (24,934–70,221 ppm) (Table S3). Monazite from the Anglès and Soulié granites has medium Th/U ratios (1.6–7.6), while monazite from the Martys granite has very high and variable Th/U ratios (4.4–50.7).

Anglès granite

Sample MN14-09 shows well-equilibrated textures and a large grain size (>1 mm). It is composed of leucocratic minerals in equal amount (quartz, plagioclase and K feldspar) and contains abundant biotite (ca. 15%). Nineteen spots on five xenotime grains (7 spots) and nine monazite grains (12 spots) were analysed (Table S3). In the Th–Pb concordia diagram, all the data are concordant to subconcordant (95–102% of concordance) around 300–310 Ma (Fig. 10a). The weighted average $^{208}Pb/^{232}Th$

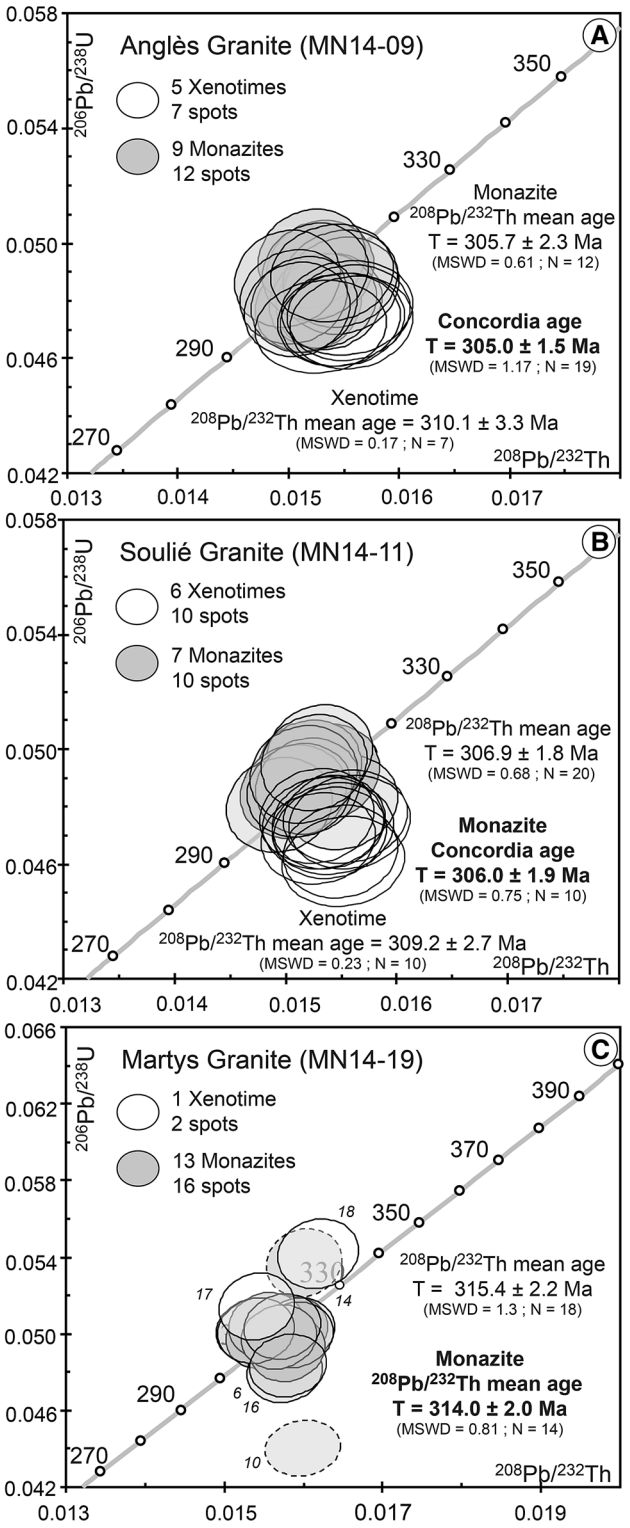

Fig. 10 Monazite and xenotime U–Th–Pb Concordia diagrams for the granites. *Error ellipses* and uncertainties in ages are ±2σ. The *stippled ellipses* are not taken into account for the age calculation and the numbers refer to analytical data in Table S3. **a** Anglès granite (MN14-09); **b** Soulié granite (MN14-11); **c** Martys granite (MN14-19)

age for the data obtained on monazite is 305.7 ± 2.3 Ma (MSWD = 0.61; N = 12), in agreement with the weighted average $^{208}Pb/^{232}Th$ age of 310.1 ± 3.3 Ma (MSWD = 0.17; N = 7) obtained on xenotime grains (Fig. 10a). This agrees well with the concordia age of 305.0 ± 1.5 Ma calculated from both xenotime and monazite data (MSWD = 1.17; N = 19) (Fig. 10a). The best age estimate is provided by the concordia age obtained on monazite and xenotime grains of 305.0 ± 1.5 Ma.

Soulié granite (MN14-11)

Sample MN14-11 shows equigranular textures with a smaller grain size (<1 mm). It is a leucogranite mostly composed of quartz, K feldspar and white micas. Plagioclase and biotite are less abundant. Ten spots on 7 monazite grains were performed. In a concordia diagram, ages are concordant (98–102% of concordance) and the concordia age is 306.0 ± 1.9 Ma (MSWD = 0.75; N = 10) (Fig. 10b, Table S3). Ellipses from 7 xenotimes are slightly discordant (93–98% of concordance) compared to ellipses of monazites. This slight discrepancy may be related to a matrix mismatch due to the use of a monazite standard. The weighted average $^{208}Pb/^{232}Th$ age for these data obtained on xenotime grains is 309.2 ± 2.7 Ma (MSWD = 0.23; N = 10), in agreement with the weighted average $^{208}Pb/^{232}Th$ age of 306.9 ± 1.8 Ma obtained to the all data (MSWD = 0.68; N = 20) (Fig. 10b). The best age estimate is provided by the concordia age of 306.0 ± 1.9 Ma obtained on monazite.

Martys granite (MN14-19)

Sample MN14-19 shows a granular texture with millimetre- sized grains that do not show any plastic deformation. It is mostly composed of quartz, K feldspar, plagioclase and biotite with rare white micas. Eighteen spots on 13 monazite crystals (16 spots) and only one xenotime (2 spots) were performed (Table S3). Except one analysis (spot 10; 87% of concordance), all ellipses are concordant to subconcordant around 305–320 Ma (96–105% of concordance). The weighted average $^{208}Pb/^{232}Th$ age for all data is 315.4 ± 2.2 Ma (MSWD = 1.3; N = 18) (Fig. 10c), in agreement with the ages given by only monazite separately. These data yield a weighted average $^{208}Pb/^{232}Th$ age of 314.0 ± 2.0 Ma (MSWD = 0.81; N = 14 (except spot 10 and 14)) and a $^{206}Pb/^{238}U$ mean age of 314.8 ± 1.6 (MSWD = 0.52; N = 12 (except spot 10, 14, 6, 16) (Fig. 10c). The best age estimate is provided by the weighted average $^{208}Pb/^{232}Th$ age of 314.0 ± 2.0 Ma obtained on monazite.

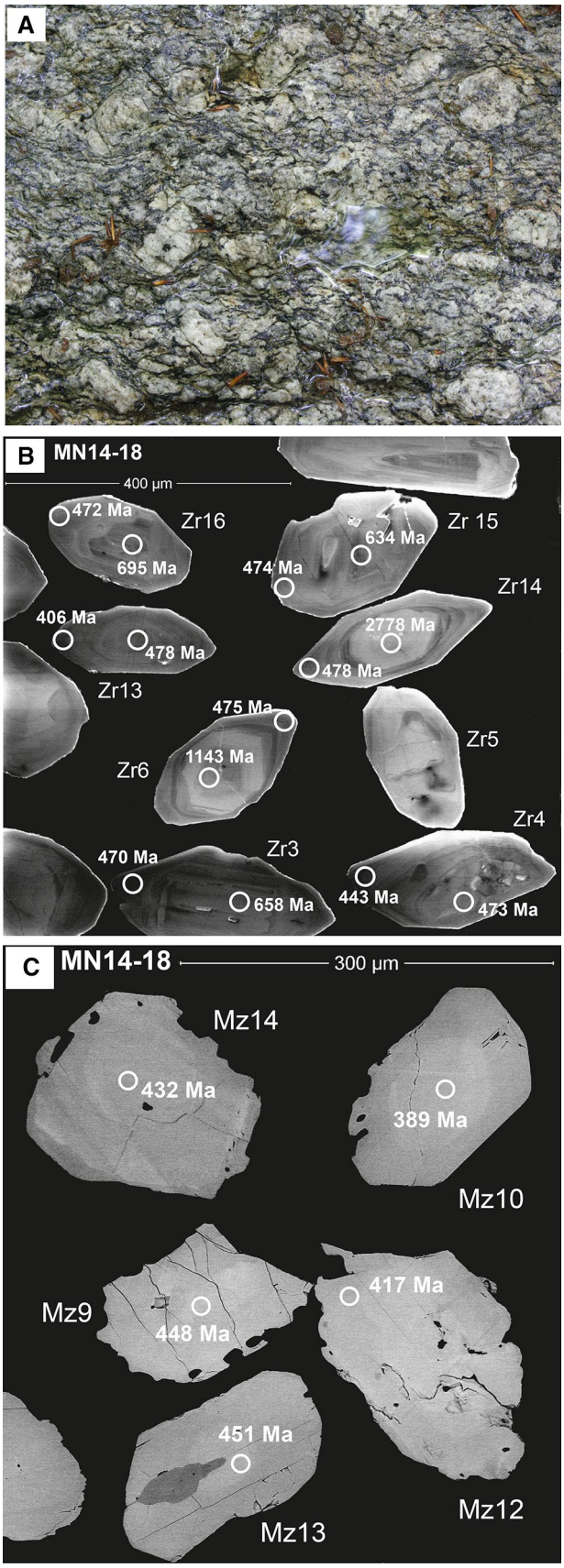

Fig. 11 **a** Hand sample photograph of the Albine orthogneiss (MN14-18) and **b**, **c** cathodoluminescence images of Zircon (Zr) and Monazite (Mz). *Circles* analytical spots with a diameter of about 21 µm (zircon) or 9 µm (monazite and xenotime). The numbers refer to analytical data in Table S3 or 2

The Albine orthogneiss MN14-18

Sample MN14-18 is located in the Nore dome (Fig. 2). It is a K feldspar porphyroclast-bearing orthogneiss (Fig. 11a) that shows a weak foliation (S2) and locally presents a constrictional fabric (Rabin et al. 2015). Grain size is bimodal but generally small (<1 mm). It is mostly composed of quartz and poikilitic K feldspar. Plagioclase is rare, and biotite is abundant (ca. 10–15%). Most of the analysed zircon grains are euhedral, transparent and colourless. Cathodoluminescence images show that most zircons have complex internal structures (sector zoning and inherited cores) (Fig. 11b). This growth zoning is characteristic of zircon grains, which crystallized from a magma (Hanchar and Miller 1993; Hoskin 2000). Thirty spots on both cores and rims of 18 zircon grains were analysed (Table 2) and plotted in the Tera–Wasserburg diagram (Fig. 12a).

Except for spot 22, which shows 19% of discordance, the data are in concordant or subconcordant positions in the range of 95–101%. Ages vary widely between 400 and 2800 Ma (Table 2; Fig. 12a). Figure 11a displays two distinct concordant populations around 600–700 and 400–500 Ma and four isolated but concordant spots (6, 10, 12 and 26) around 850 Ma, 1.2, 1.8 and 2.8 Ga. These isolated spots have Th/U ratios ranging between 0.12 and 0.67 and they correspond to magmatic inherited cores (Fig. 11b; Table 2). The cluster around 650 Ma is composed of six concordant cores (4, 8, 14, 16, 20 and 25). These six data points have similar Pb, U and Th concentrations (about 4–39, 34–329 and 11–282 ppm respectively). Their Th/U ratios range between 0.3 and 2.07.

The youngest population around 400–500 Ma is the most important one (19 analyses). It is constituted by 12 rims and seven cores. Except spot 26 (rim of zircon 50), all the analysed rims in this study belong to this group. Among these 19 analyses, 11 rims and three cores have low Th/U ratios ranging between 0.03 and 0.1 with homogeneous Pb (4–52 ppm), Th (10–33 ppm) and U (189–873 ppm) concentrations. Other analyses constituted by four cores and one rim show higher Th/U ratios (0.15–1.42) due to their more important Th contents (29–560 ppm). The Pb (13–37 ppm) and U (183–394 ppm) contents are similar to other data points of this group. Among these 19 points, 16 have a concordant position (99–101%) and yield a concordia age of 472.1 ± 2.8 Ma (MSWD = 0.96) (Table 2;

Table 2 Analytical results of LA-ICP-MS U–Pb zircon dating of Albine granite (MN14-18)

Spot	Concentration (ppm)			Th/U	Raw ratios				Rho	Apparent age (Ma)		Conc. (%)
	Pb	Th	U		$^{207}Pb/^{235}U$	$\pm 2\sigma$	$^{206}Pb/^{238}U$	$\pm 2\sigma$		$^{206}Pb/^{238}U$	$\pm 2\sigma$	
1. Z 4r	25	11	377	0.03	0.576	0.017	0.0711	0.0020	0.91	443	12	96
2. Z 4c	37	560	394	1.42	0.587	0.017	0.0760	0.0021	0.95	473	12	101
3. Z 3r	16	20	219	0.09	0.603	0.018	0.0766	0.0021	0.91	476	13	99
4. Z 3c	10	60	83	0.73	0.983	0.033	0.1074	0.0030	0.81	658	17	95
5. Z 2r	45	13	646	0.02	0.584	0.017	0.0756	0.0020	0.95	470	12	101
6. Z 2c	6	5	45	0.12	1.317	0.043	0.1409	0.0039	0.83	850	22	100
7. Z 7r	14	19	189	0.10	0.603	0.018	0.0769	0.0021	0.90	478	13	100
8. Z 7c	9	28	95	0.30	0.798	0.027	0.0968	0.0027	0.82	596	16	100
9. Z 6r	34	24	482	0.05	0.593	0.017	0.0764	0.0021	0.94	475	12	100
10. Z 6c	39	86	193	0.45	2.073	0.059	0.1939	0.0053	0.95	1143	28	100
11. Z 14r	30	21	426	0.05	0.593	0.017	0.0769	0.0021	0.94	478	12	101
12. Z 14c	32	33	50	0.67	14.641	0.411	0.5386	0.0146	0.97	2778	61	99
13. Z 15r	21	15	299	0.05	0.596	0.017	0.0762	0.0021	0.93	474	12	100
14. Z 15c	39	282	329	0.86	0.866	0.025	0.1033	0.0028	0.94	634	16	100
15. Z 16r	14	29	197	0.15	0.592	0.018	0.0760	0.0021	0.89	472	12	100
16. Z 16c	18	221	106	2.07	1.003	0.033	0.1138	0.0031	0.84	695	18	98
17. Z 13r	52	17	873	0.02	0.509	0.015	0.0649	0.0017	0.92	406	11	97
18. Z 13c	17	50	227	0.22	0.601	0.018	0.0769	0.0021	0.91	478	12	100
19. Z 12r	29	28	408	0.07	0.581	0.017	0.0755	0.0020	0.92	469	12	101
20. Z 12c	4	11	34	0.32	0.921	0.038	0.1092	0.0031	0.67	668	18	101
21. Z 45r	27	22	383	0.06	0.595	0.017	0.0760	0.0020	0.93	472	12	100
22. Z 45c	*84*	*167*	*444*	*0.38*	*2.655*	*0.076*	*0.1791*	*0.0048*	*0.95*	*1062*	*26*	*81*
23. Z 44c	34	16	541	0.03	0.541	0.017	0.0688	0.0019	0.88	429	11	98
24. Z 46r	23	10	325	0.03	0.594	0.017	0.0767	0.0021	0.92	476	12	101
25. Z 46c	28	222	236	0.94	0.842	0.025	0.1009	0.0027	0.90	620	16	100
26. Z 50c	96	145	276	0.53	5.140	0.144	0.3185	0.0086	0.96	1782	42	97
27. Z 25c	18	15	249	0.06	0.589	0.018	0.0761	0.0020	0.88	473	12	100
28. Z 10c	24	33	342	0.10	0.593	0.018	0.0761	0.0021	0.88	473	12	100
29. Z 11c	20	57	267	0.22	0.596	0.018	0.0758	0.0020	0.88	471	12	99
30. Z 9c	13	32	183	0.18	0.587	0.018	0.0761	0.0020	0.89	473	12	101

Italics represents discordant data (±5% of discordance)

r rim, *c* core

Fig. 12a). Spots 1, 17 and 23 plot slightly below the concordia line (96–98% of concordance) showing younger ages (406, 429 and 443 Ma), probably due to radiogenic Pb loss (Table 2).

The majority of monazite grains are subhedral, transparent and yellow and 150–200 µm in size (Fig. 11c). All have uniformly low Th/U ratios (0.2–0.8) with low–medium Pb (184–365 ppm) and medium Th (1584–2419 ppm) and U (2197–7758 ppm) contents. A total of 20 spots on 15 monazite grains were performed, plotted in the concordia diagram, the ellipse are concordant (100–104% of concordance). The heterogeneous $^{208}Pb/^{232}Th$ ages ranging from 331 ± 8 to 479 ± 12 Ma correspond to variation from one grain to another as well as heterogeneities within single crystals (Table S3; Fig. 12b). In the concordia diagram, most data ($N = 16$) plot between 420 and 480 Ma. Among these data, the eight ellipses (spot 2, 3, 9, 10, 11, 18, 19 and 20), which have the oldest $^{208}Pb/^{232}Th$ ages, yield a concordia age of 470.4 ± 4.7 Ma (MSWD = 2; $N = 8$). In the concordia diagram, the white ellipses correspond to 12 analyses, which are probably without significance. They correspond to a Pb loss or an analytical mixture between an old domain (470 Ma) and younger domain probably Variscan (<330 Ma) (Table S3; Fig. 12b). This age of 470.4 ± 4.7 Ma is similar within errors to the concordia age of 472.1 ± 2.8 Ma obtained on zircon grains.

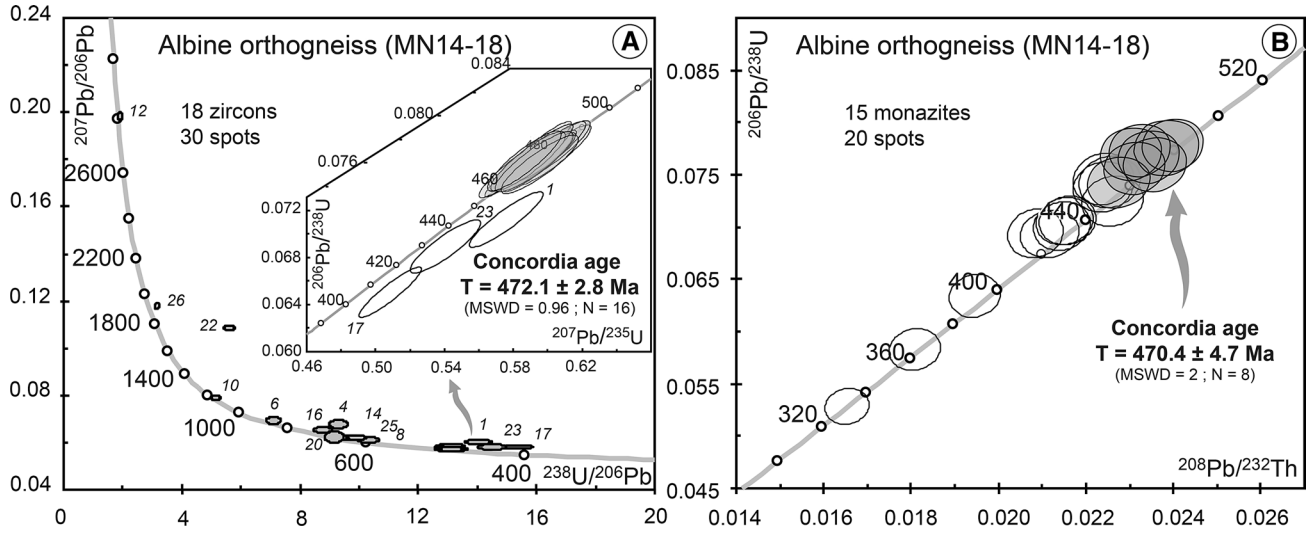

Fig. 12 U–Th–Pb diagrams obtained with LA-ICMPS for the Albine orthogneiss (MN14-18). *Error ellipses* and uncertainties in ages are ±2σ. The *white ellipses* are not taken into account for the age calculation and the numbers refer to analytical data in Table 2. **a** Zircon Tera–Wasserburg diagram and a Concordia diagram detailed around 450 Ma. **b** Monazite U–Th–Pb Concordia diagram

Interpretation of age data

Ordovician inheritance (the Albine orthogneiss)

In the Nore dome, the Albine orthogneiss (MN14-18) was dated by U–Th–Pb LA-ICP-MS on zircon and monazite grains. Sixteen zircon analyses yield a concordia age of 472.1 ± 2.8 Ma. The absence of Variscan dates associated with the concordant position of the majority of the data points on the concordia plot suggests that the 472.1 ± 2.8 Ma zircon date is the intrusion age for the protolith of the Albine orthogneiss. This age is similar within errors to the concordia age of 470.4 ± 4.7 Ma obtained on monazite grains. We interpret these Ordovician ages as the magmatic crystallization age of zircon and monazite, and therefore the emplacement age of the Albine granite. This Ordovician event has also been interpreted as the emplacement age of the protolith of the augen gneiss of the Caroux and Espinouse domes (Ducrot et al. 1979; Roger et al. 2004, 2015; Cocherie et al. 2005; Faure et al. 2010; Pitra et al. 2012). Rare inherited zircon cores indicate the occurrence of several older proterozoic magmatic events in the Montagne Noire (850 Ma, 1.2, 1.8 and 2.8 Ga). The Albine orthogneiss shows a vertical and weak foliation that trends E–W and corresponds to the D2 deformation. The absence of Variscan monazite ages suggests the absence of late orogenic resetting. The preservation of the Ordovician monazites confirms that this mineral may be highly resistant to high-temperature processes (Didier et al. 2013).

Age of migmatization within the MNAZ core

Along the D2 high-strain corridor near La Salvetat, migmatitic sample MN13-B2 is dated on monazite and xenotime at 307.6 ± 1.8 Ma. We interpret this age as high-temperature metamorphism M2 occurring under suprasolidus conditions and coeval to D2 deformation. In the north-eastern part of the Espinouse dome at the S1/S3 transition, sample MNC04 yields an age at 307.7 ± 2.5 Ma (on monazite and xenotime) that is interpreted as the best estimation of the peak temperature metamorphic age under suprasolidus conditions synchronous to D3 (Fig. 2a; Table 1).

The two metatexites east of the Cabot village, sample MN9-B1 and MN14-04B, yield similar concordia ages at ca. 304.7 ± 1.7 and 301.5 ± 1.4 Ma on monazite (Fig. 2a; Table 1). Both rocks show D3 fabrics with a migmatitic foliation that dips weakly towards the east. We interpret these two ages as the best estimation for LP–HT metamorphism at suprasolidus conditions synchronous to D3. The Cabot metatexite MN14-04B dated at 301.5 ± 1.4 Ma is crosscut by the Cabot cordierite-bearing granitic dyke (MN14-04C) dated at 312.1 ± 1.8 Ma. As described above, the field structural relationships indicate that the age does not correspond to the crystallization age associated with dyke intrusion. We suggest that this age is inherited from an early melting event taking place deeper in the crust or from prograde metamorphism under amphibolite facies conditions. Indeed, within peraluminous magmas, as the cordierite-bearing Cabot granite, the solubility of monazite might be very low (Montel 1993).

Age of metamorphism within unmolten metasedimentary rocks

The La Fage paragneiss (MN14-03) located within the D3 transition zone and near the anatectic front (Fig. 2) shows two populations of monazites with different ages (Table 1). The $^{208}Pb/^{232}Th$ mean age of 305.7 ± 3.9 Ma is interpreted as the age of peak temperature metamorphism synchronous with D3 development. The age is similar to the 307.7 ± 2.5 and 307.6 ± 1.8 Ma ages of obtained for the Espinouse migmatite (MNC04) and the La Salvetat migmatite (MN13-B2). A younger event is recorded at 284 ± 13 Ma that we interpret as late deformation and fluid circulation during retrograde evolution (Table 1).

The Saint-Pons-de-Thomières staurolite-bearing micaschists, samples MN14-15b and MN22-A1, yield concordia ages of 312.1 ± 2.1 and 309.0 ± 3.1 Ma, respectively. These two ages are similar within error and are interpreted as the crystallization age of monazite at peak temperature conditions synchronously to the onset of D2 deformation (Table 1; Fig. 7).

Emplacement of the syn-kinematic granites

The monazite grains from the Martys granite give a weighted average $^{208}Pb/^{232}Th$ age of 314.0 ± 2.0 Ma that we interpret as the emplacement age of the Martys granite. Field observations suggest that the Martys granite is syn-kinematic and emplaced within the D2 corridor and the D3 transition zone (Rabin et al. 2015, Fig. 2; Table 1). This suggests that D2 and D3 were synchronous in time around 314 Ma. The Soulié and Anglès granites are also syn-kinematic and emplaced along the dextral high-strain D2 corridor at 306 ± 1.9 and 305 ± 1.5 Ma, respectively. This may indicate that D2 lasted until 305 Ma.

Summary of Variscan ages within the tectono-metamorphic framework

Our geochronological results can be summarized as follows (Table 1):

- The unmolten St Pons micaschists (MN22-A1 and MN14-15b) are dated between ca. 315–306 Ma considering the age uncertainties. This period corresponds to the timing of peak temperature metamorphism during D2 deformation along the southern flank of the MNAZ with the onset of D2 at ca. 315 Ma (Table 1). Along the eastern termination of the dome, the unmolten paragneiss MN14-03 yields an age of 306 ± 4 Ma interpreted as the age of D3 deformation that corresponds to vertical shortening with a preferential ca. E–W-directed stretching (Rabin et al. 2015).
- The migmatitic rocks are dated between ca. 314–303 Ma. This period corresponds to the timing of D2 (MN13B2; 310–305 Ma) and D3 (MN9-B1, MN14-04C and MNCO4; 314–303 Ma; Table 1) that were coeval but partitioned within the crust as suggested by Rabin et al. (2015).
- The late orogenic syn-kinematic granites, Martys, Soulié and Anglès, are dated at ca. 316–303 Ma (Table 1). These three granites emplaced during D2 within the S2 high-strain corridor whereas the surrounding rocks were partially molten.

Discussion

Within the MNAZ two tectono-metamorphic events are classically proposed, (1) a D1/M1 event that corresponds to a barrovian MP/MT metamorphism during crustal thickening in response to southward nappe stacking and (2) a D2/M2 event that corresponds to LP/HT metamorphism during dome formation and subsequent crustal thinning (e.g. Faure et al. 2010). Partial melting may have started at the end of prograde metamorphism (D1/M1 event) and was probably coeval with the onset of D2 deformation (Rabin et al. 2015). D2 and D3 developed synchronously after the onset of partial melting in the middle crust (Rabin et al. 2015). Deformation partitioning leads to the appearance of D2 transpression in the lower and partially molten crustal levels. This was coeval with D3 along strike extension in the upper crustal levels. In the following, we first discuss the timing of migmatization and plutonism during D2/M2. Afterwards, we start deciphering the D1/M1 history responsible for thickening of the variscan crust before exhumation of the migmatitic dome. Nevertheless, the scarcity of data makes this point speculative.

Timing of partial melting and plutonism during dome emplacement

Figure 13 is a synoptic P–T diagram that summarizes the P–T estimations of Rabin et al. (2015), Whitney et al. (2015) and Fréville et al. (2016). On this diagram we have added our new geochronological results. The shape of the P–T path after peak pressure is well constrained by quantified peak and retrograde P–T conditions. The peak temperature conditions ranging 700–750 °C correspond to those of the partially molten rocks during the M2 (blue and purple paths on Fig. 13).

Recently, Roger et al. (2015) bracketed the high-temperature M2/D2 event and anatectic granite emplacement at ~310–300 Ma, 20 Myr after the proposed timing for LP/HT M2/D2 event constrained by Faure et al. (2010) at 333–318 Ma. In accordance with Roger et al. (2015), our U–Th–Pb results from metatexites (MN14-04B, MN9-B1 and

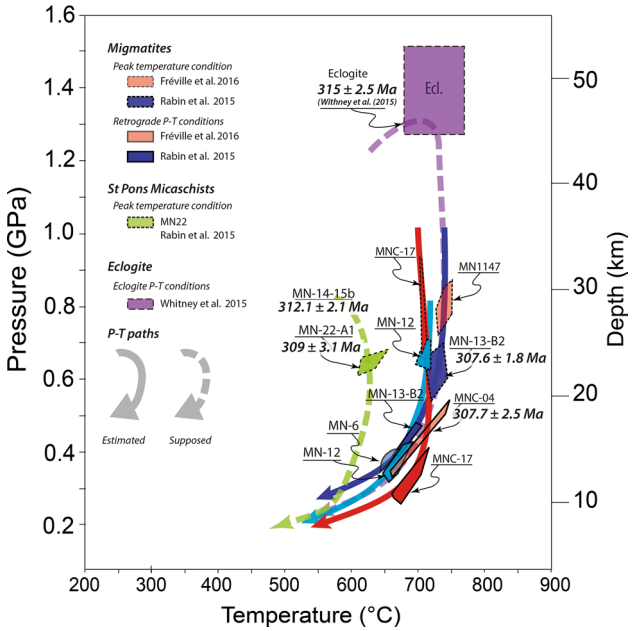

Fig. 13 Summary of quantified P–T estimations (from literature) and related ages (this study) within the MNAZ

MNC04) range 310–300 Ma (Table 1). We interpret this age range as the peak temperature under suprasolidus conditions. The onset of partial melting may have started diachronously depending on the depth of migmatization. The timing of the onset of partial melting may be approached considering the age of anatectic magmatism. Faure et al. (2010, 2014) suggested that aluminous and peraluminous anatectic plutonism took place at ca. 333–326 Ma and late granitoids emplaced at ca. 325–318 Ma. These authors reported EPMA ages at 325 ± 7 and 318 ± 4 Ma for the Anglès and Soulié granites, respectively. Our results indicate emplacement ages for the Anglès, the Soulié and the Martys granites at 305 ± 2, 306 ± 2 and 314 ± 2 Ma, respectively (Table 1). This age at 314 ± 2 Ma could be considered as the minimum age for the onset of partial melting. This is in accordance with the monazite ages of 312.1 ± 1.8 Ma reported within the Cabot cordierite-bearing granitic dyke (MN14-04C) (Table 1). The recent geochronological studies on the Montagne Noire show that whatever the analytical technique used (TIMS or LA-ICP-MS) and the minerals dated (monazite, xenotime or zircon), the 330–320 Ma ages obtained by EPMA dating of monazite by Faure et al. (2010) have not been confirmed by the other studies (Poilvet et al. 2011; Franke et al. 2011; Pitra et al. 2012; Roger et al. 2015; Whitney et al. 2015). We believe that these EPMA results may be biased considering that this method does not measure isotopic ratios but U, Th and Pb concentrations. Our results show that the presence of not only inherited Pb (^{208}Pb) but also common Pb (^{204}Pb) within the Pb content measured in the monazite of the Montagne Noire cannot be excluded and might be responsible for these old 330–320 Ma ages obtained by the EPMA approach.

Our results suggest that partial melting may have started at ca. 315 Ma and lasted 15–10 Myr. Our ages are coherent with the U–Th–Pb ages recently proposed by Poilvet et al. (2011), Franke et al. (2011), Pitra et al. (2012) and Roger et al. (2015) showing the same 315–300 time span. These results are consistent with the Montagne Noire migmatite dome emplaced at 315–300 Ma during which migmatization and plutonism were synchronous, in agreement with Whitney et al. (2015) and Roger et al. (2015).

P–T–t-D evolution: from crustal thickening to exhumation

Between 315 and 300 Ma the MNAZ middle crust was partially molten. Its thermal state is defined as isothermal with temperature around 700 °C (Fig. 13) and may be compared to a portion of the melt-enhanced geotherm as defined by Depine et al. (2008). Indeed, within the given 15 Myr time span, partial melting and magma transfer through the crust may have produced a transient diffusive heat relaxation and advection that is illustrated as a steady-state melt-enhanced geotherm (Depine et al. 2008).

In their model, Depine et al. (2008) consider a fluid-absent amphibolite middle and lower crust in the calculation of the melt-enhanced geotherm. The obtained melt-enhanced geotherm shows temperature culminating at 850 °C that was attained 25–35 Ma after crustal thickening. Depine et al. (2008) suggest that taking into account of a mica-rich lithology or a fluid-present composition, as it is the case for the MNAZ (Rabin et al. 2015; Fréville et al. 2016), melting would start at lower temperatures and earlier during thermal relaxation. In the MNAZ, the peak temperature that corresponds to the melt-enhanced geotherm from eclogite to low-pressure granulite pressure conditions is buffered at 720 °C (Fig. 13). Therefore, one may consider that this 720 °C peak temperature was reached in a period shorter than the 25–35 Ma needed to attain a melt-enhanced geotherm buffered at 850 °C (Depine et al. 2008). However, resolving the timing of thermal relaxation is not straightforward and additional data on prograde metamorphism are needed.

In order to discuss the timing of the D1/M1 event responsible for crustal thickening, we envisage the scenario shown in Fig. 14. On this figure three semi-quantitative P–T–t paths are drawn for three rocks initially located at different depths: an eclogite boudin, an unmolten micaschist (MN22) and a migmatitic gneiss (MNC04). The shape of these P–T paths after peak pressure is quite well documented by P–T estimations from migmatites (Fig. 13). The shape of the prograde path that may correspond to D1/M1, is not constrained due to the lack of quantified P–T

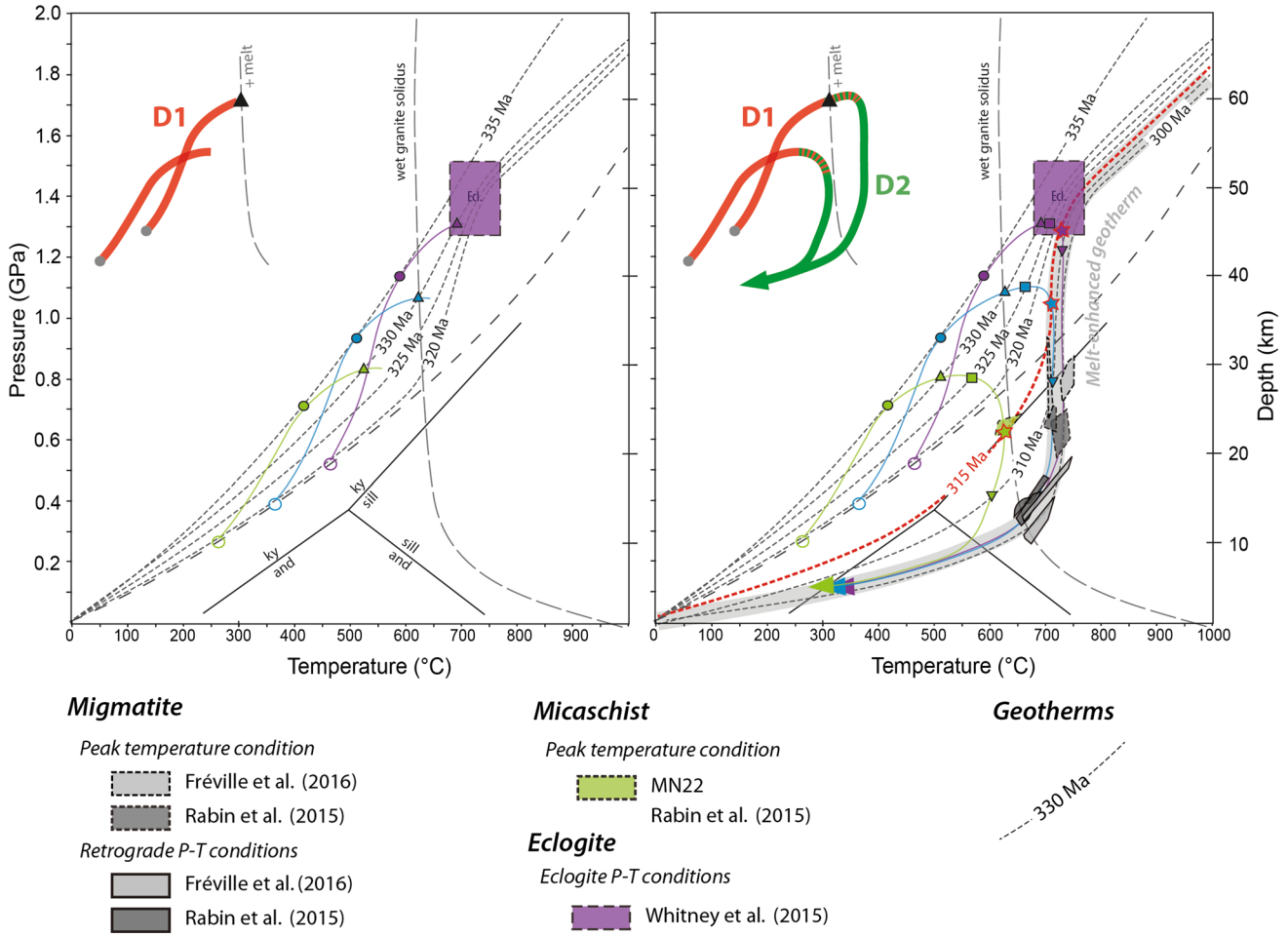

Fig. 14 Prospective scenario showing three semi-quantitative P–T–t-D paths are drawn for three rocks that were located at different initial depths: an eclogite boudin, an unmolten micaschist (MN22) and a migmatitic gneiss (MNC04). The melt-enhanced geotherm is modified after Depine et al. (2008). The long-dashed line corresponds to the initial geotherm. The *thick green* and *red lines* represent the P–T evolutions of D1 and D2, respectively, for rocks that recorded melting or not. See text for details

results, but is typical of a thickened crust involved in a collisional orogen. Several occurrences of eclogites are documented within the MNAZ (Demange 1985; Alabouvette et al. 2003; Whitney et al. 2015). Recently, the study of the Terme de Fourcaric eclogite yields P–T conditions of ca. 1.4 GPa and 725 ± 25 °C (Whitney et al. 2015) that are similar to the recalculated P–T conditions for the Carbardès and Le Jounié eclogites (Demange 1985; Franke et al. 2011) (Fig. 1b for location). We consider that these eclogitic conditions correspond to peak pressure conditions. Considering this upper pressure limit we can infer the prograde portion of a P–T path typical for crustal thickening (ca. 20 °C/km; Fig. 14). The green path shows the possible metamorphic evolution recorded by the St Pons micaschists, which culminated at peak temperature conditions of 0.65 ± 0.05 GPa and 630 ± 20 °C (Rabin et al. 2015). The blue and purple paths show the possible evolution of two migmatitic rocks within the MNAZ. The purple path reaches eclogite facies conditions defined by Whitney et al. (2015).

Faure et al. (2014) determined a Sm–Nd isochron age of 358 ± 9 Ma for a Peyrambert eclogite boulder and monazite EPMA U–Th–Pb_{tot} ages between 357 ± 10 and 352 ± 10 Ma within peraluminous paragneisses also called kinzigites (i.e. metapelitic metatexites in this study). They have also presented U–Pb SHRIMP and SIMS ages for zircon and rutile of 314 ± 2.5, 311 ± 2 and 308 ± 4 Ma for the Peyrambert eclogite. Because these U–Pb ages obtained on the eclogite were younger than ages obtained on the migmatites and granites (333–318 Ma; Faure et al. 2010), they interpreted this 360 Ma age as the timing of the high-pressure metamorphism (M1) and the younger age around 315–310 Ma as a hydrothermal event. Whitney et al. (2015) presented a robust LA-ICP-MS age for eclogite at 315.2 ± 1.6 Ma with four ellipses yielding an older age at 359.5 ± 4.7 Ma. Based on garnet zoning and

inclusion suites, rutile texture and Zr zoning, P–T results, and the REE signature determined for dated zircon, Whitney et al. (2015) interpreted the 315 Ma age as the age of the eclogite facies metamorphism (M1) and the 360 Ma as a pre-eclogite facies (likely amphibolite) metamorphism, corresponding to crystallization of the zircon under lower-pressure plagioclase-stable conditions. In this study, in the micaschists MN14-15b some data form a cluster around 360 Ma that might correspond to an early metamorphic event, but the strong scattering of data prevents the calculation of a reliable age.

In agreement with Whitney et al. (2015), we interpret the 315 Ma age as the age of the eclogitic metamorphism, which corresponds to the peak pressure and temperature at ~1.4 GPa and ~720 °C. At these P–T conditions the surrounding orthogneisses are partially molten supposing the possibility of fluid-present melting (Hasalová et al. 2008) (Fig. 13). This time range (315–314 Ma) is very similar within error to the age of 312.1 ± 2.1 Ma recorded in the St Pons micaschist (MN14-15b) for the peak temperature condition at 660 °C (Fig. 13). Thus a geotherm at ~315 Ma is likely to be defined (Fig. 14). The syn-thickening prograde history before 315 Ma remains poorly documented. Still, a first-order guess could be given by considering the position of former geotherms in the P–T diagram as proposed in Fig. 14. We could propose that crustal thickening during nappe stacking may occur around ~330–340 Ma or before. Charles et al. (2009) proposed that thrust nappes emplacement may have occurred at 340–325 Ma. However, the position of the geotherms before 315 Ma is highly speculative and a new modelling of the thermal evolution considering a micaceous crust is needed. In addition, the model shown on Fig. 14 is no more applicable if one considers horizontal flow of the partially molten crust as suggested by Whitney et al. (2015). Finally, more P–T–t data and new modelling of thermal relaxation of a micaceous crust are needed in order to track the record of syn-thickening prograde metamorphism within the MNAZ.

Conclusion

This geochronological study allows unravelling three major points about the tectono-thermal evolution of the MNAZ. Partial melting started at ca. 315 Ma and lasted until 303 Ma. This 315–303 Ma period corresponds to the timing of D2 and D3 that were synchronous but spatially partitioned within the crust. Peak temperature assemblage within micaschists was dated at 315–306 Ma. The late orogenic syn-kinematics granites, Martys, Soulié and Anglès, emplaced within the S2 high-strain corridor at ca. 316–303 Ma whereas the surrounding rocks were partially molten. Further P–T–t analyses are needed to precisely constrain the timing of D1 deformation related to nappe stacking and crustal thickening in the MNAZ.

Acknowledgements This research was financially supported by an INSU/SYSTER project from French CNRS. This research was also partly supported by the French RENATECH network, who provided access to the electron microscope of the MIMENTO platform of the University of Bourgogne-Franche-Comté. Authors are very grateful for the constructive comments made by Pavel Pitra, Patrice Rey and Romain Tartèse that helped to improve the manuscript.

References

Aerden DGAM (1998) Tectonic evolution of the Montagne Noire and a possible orogenic model for syncollisional exhumation of deep rocks, Variscan belt, France. Tectonics 17:62–79

Aerden DGAM, Malavieille J (1999) Origin of a large-scale fold nappe in the Montagne Noire, Variscan belt, France. J Struct Geol 21:1321–1333

Alabouvette B, Demange M, Guérangé-Lozes J, Ambert P (2003) Notice et carte géologique de la France (1/250000) feuille de Montpellier. BRGM, Orléans, p 164

Arthaud F (1970) Etude tectonique et microtectonique comparée de deux domaines hercyniens: les nappes de la Montagne Noire (France) et l'anticlinorium de l'Iglesiente (Sardaigne). Université des Sciences et Techniques du Languedoc, p 175

Ayers JC, Miller C, Gorisch B, Milleman J (1999) Textural development of monazite during high-grade metamorphism: hydrothermal growth kinetics, with implications for U–Th–Pb geochronology. Am Mineral 84:1766–1780

Ballèvre M, Fourcade S, Capdevila R, Peucat JJ, Cocherie A, Fanning CM (2012) Geochronology and geochemistry of Ordovician felsic volcanism in the Southern Armorican Massif (Variscan belt, France): implications for the breakup of Gondwana. Gondwana Res 21:1019–1036

Bard JP, Rambeloson R (1973) Métamorphisme plurifacial et sens de variation du degrès géothermique durant la tectogenèse polyphasée hercynienne dans la partie orientale de la zone axiale de la Montagne Noire (massif du Caroux, sud du Massif Central français). Bull Soc Geol Fr 15:579–586

Brun JP, Van Den Driessche J (1994) Extensional gneiss domes and detachment fault systems: structure and kinematics. Bull Soc Geol Fr 165(6):519–530

Brun JP, Van Den Driessche J (1996) Réponse à observations et remarques sur l'article "Extensional gneiss domes and detachment fault systems/structure and kinematics (Brun JP, Van Den Driessche J (1994) Bull Soc Géol Fr 165 (6): 519–530)". Bull Soc Geol Fr 167(2):295–302

Charles N, Faure M, Chen Y (2009) The Montagne Noire migmatitic dome emplacement (French Massif Central): new insights from petrofabric and AMS studies. J Struct Geol 31(11):1423–1440

Cocherie A, Baudin T, Autran A, Guerrot C, Fanning M, Laumonier B (2005) U–Pb zircon (ID-TIMS and SHRIMP) evidence for the early Ordovician intrusion of metagranites in the late Proterozoic Canaveilles Group of the Pyrenees and the Montagne Noire (France). Bull Soc Geol Fr 176:269–282

Demange M (1985) The eclogite-facies rocks of the Montagne-Noire, France. Chem Geol 50:173–188. doi:10.1016/0009-2541(85)90119-6

Demange M (1993) What does the Monts-De-Lacaune Fault (Montagne-Noire, France) mean—implications for the origin of the Nappes. C R Acad Sci Ser II 317(3):411–418

Demange M (1994) AnteVariscan evolution of the Montagne-Noire (France)—from a passive margin to a foreland basin. C R Acad Sci Ser II 318(7):921–933

Demange M (1996) Extensional gneiss domes and detachment fault systems: structure and kinematics—observations and remarks. Bull Soc Geol Fr 167(2):295–298

Demange M (1998) Contribution au problème de la formation des dômes de la Zone axiale de la Montagne Noire: analyse géométrique des plissements superposés dans les séries métasédimentaires de l'enveloppe. Implications pour tout modèle géodynamique. Géol Fr 4:3–56

Demange M (1999) Evolution tectonique de la Montagne Noire: un modèle en transpression. C R Acad Sci Paris 329:823–829

Depine GV, Andronicos CL, Phipps-Morgan J (2008) Near-isothermal conditions in the middle and lower crust induced by melt migration. Nat Geosci 452:80–83

Didier A, Bosse V, Cherneva P, Gautier P, Georgieva M, Paquette JL, Gerdjiko I (2013) Syn-deformation fluid-assisted growth of monazite during renewed high-grade metamorphism in metapelites of the Central Rhodope (Bulgaria, Greece). Chem Geol 381:206–222

Doublier MP, Potel S, Wemmer K (2014) The tectono-metamorphic evolution of the very low-grade hanging wall constrains two stages gneiss dome formation in the Montagne Noire example (S-France). J Metamorph Geol 33:71–89. doi:10.1111/jmg.12111

Ducrot J, Lancelot JR, Reille JL (1979) Datation en Montagne Noire d'un témoin d'une phase majeure d'amincissement crustal caractéristique de l'Europe prévarisque. Age of a major phase of crustal thinning characteristic of PreVariscan Europe determined in the Montagne Noire region. Bull Soc Geol Fr 21(4):501–505

Echtler H, Malavieille J (1990) Extensional tectonics, basement uplift and Stephano–Permian collapse basin in a late Variscan metamorphic core complex (Montagne Noire, southern Massif Central). Tectonophysics 177:125–138

Engel W, Feist R, Franke W (1978) Syn-orogenic gravitational transport in the Carboniferous of the Montagne Noire (South France). Z dt geol Ges 129:461–472

Engel W, Feist R, Franke W (1980) Le Carbonifère anté-Stéphanien de la Montagne Noire: rapport entre mise en place des nappes et sédimentation. Bull Bur Rech Géol Min 1(4):341–389

Faure M, Cottereau N (1988) Données cinématiques sur la mise en place du dôme migmatitique carbonifère moyen de la zone axiale de la Montagne Noire (Massif Central, France). C R Acad Sci Paris 307:1787–1794

Faure M, Lardeaux JM, Ledru P (2009) A review of the pre-Permian geology of the Variscan French Massif Central. C R Geosci 341:202–213

Faure M, Cocherie A, Bé Mézène E, Charles N, Rossi P (2010) Middle Carboniferous crustal melting in the Variscan belt: new insights from U–Th–Pb tot monazite and U–Pb zircon ages of the Montagne Noire Axial Zone (southern French Massif Central). Gondwana Res 18:653–673

Faure M, Cocherie A, Gaché J, Esnault C, Guerrot C, Rossi P, Lin W, Li Q (2014) Middle Carboniferous intracontinental subduction in the outer zone of the Variscan belt (Montagne Noire Axial Zone, French Massif Central): multimethod geochronological approach of polyphase metamorphism. Geol Soc Lond Spec Publ. doi:10.1144/SP405.2

Feist R, Galtier J (1985) Découverte de flores d'âge namurien probable dans le flysch à olistolites de Cabrières (Hérault). Implication sur la durée de la sédimentation synorogénique dans la Montagne Noire. Comptes Rendus de l'Académie des sciences, Paris, Série IIa 300:207–212

Franke W, Doublier MP, Klama K, Potel S, Wemmer K (2011) Hot metamorphic core complex in a cold foreland. Int J Earth Sci (Geol Rundsch). doi:10.1007/s00531-010-0512-7

Fréville K, Cenki-Tok B, Trap P, Rabin M, Leyreloup A, Régnier JL, Whitney D (2016) Thermal interaction of middle and upper crust during gneiss dome formation: example from the Montagne Noire (French Massif Central). J Metamorph Geol 34:447–462. doi:10.1111/jmg.12188

Gebauer D, Grünenfelder M (1982) Geological development of the Hercynian belt of Europe based on age and origin of high grade and high pressure mafic and ultramafic rocks. In: First international conference on geochronology, cosmochronology, isotope geology, Nikko, pp 111–112

Gèze B (1949) Etude géologique de la Montagne Noire et des Cévennes méridionales. Soc Géol Fr Mém 62:1–125

Guy A, Edel JB, Schulmann K, Tomek C, Lexa O (2011) A geophysical model of the Variscan orogenic root (Bohemian Massif): implications for modern collisional orogens. Lithos 124:144–157

Hamet J, Allegre C (1976) Hercynian orogeny in Montagne Noire (France)—application of Rb-87-Sr-87 systematics. Geol Soc Am Bull 87(10):1429–1442

Hanchar JM, Miller CF (1993) Zircon zonation patterns as revealed by cathodoluminescence and backscattered electron images: implication for interpretation of complex crustal histories. Chem Geol 110:1–13

Hasalová P, Schulmann K, Leka O, Stípská P, Hrouda F, Ulrich S, Haloda J, Týcová P (2008) Origin of migmatites by deformation-enhanced melt infiltration of orthogneiss: a new model based on quantitative microstructural analysis. J Metamorph Geol 26:29–53

Hoskin PWO (2000) Patterns of chaos: fractal statistics and the oscillatory chemistry of zircon. Geochim Cosmochim Acta 64:1905–1923

Hurai V, Paquette JL, Huraiovà M, Konecny P (2010) U–Th–Pb geochronology of zircon and monazite from syenite and pincinite xenoliths in Pliocene alkali basalts of the intra-carpathian back-arc basin. J Volcanol Geotherm Res 198:275–287

Jackson SE, Pearson NJ, Griffin WL, Belousova EA (2004) The application of laser ablation-inductively coupled plasma mass spectrometry to in situ U–Pb zircon geochronology. Chem Geol 211:47–69

Jaffey AH, Flynn KF, Glendenin LE, Bentley WC, Essling AM (1971) Precision measurement of half-lives and specific activities of 235U and 238U. Phys Rev C 4:1889–1906

Lardeaux JM (2014) Deciphering orogeny: a metamorphic perspective. Examples from the European Alpine and Variscan belts. Part II. Variscan metamorphism in the French Massif Central—a review. Bull Soc Géol Fr 185:281–310

Ledru P, Lardeaux JM, Santallier D, Autran A, Quenardel JM, Floch JP, Lerouge G, Maillet N, Marchand J, Ploquin A (1989) Où sont les nappes dans le Massif central français? (Where are the nappes in the French Massif central?). Bull Soc Géol Fr 3:605–618

Ludwig KR (2001) User manual for Isoplot/Ex rev. 2.49. A geochronological toolkit for Microsoft Excel. Berkeley Geochronology Center Special Publication 1a, pp 1–56

Malavieille J (2010) Impact of erosion, sedimentation, and structural heritage on the structure and kinematics of orogenic wedges: analog models and case studies. Geol Soc Am 20:4–10. doi:10.1130/GSATG48A.1

Maluski H, Costa S, Echtler H (1991) Late Variscan tectonic evolution by thinning of earlier thickened crust: a 40Ar–39Ar study of the Montagne Noire, southern Massif Central, France. Lithos 26(3–4):287–304

Matte P, Lancelot J, Mattauer M (1998) La Zone axiale hercynienne de la Montagne Noire n'est pas un "metamorphic core complex" extensif mais un anticlinal post-nappe à coeur anatectique. Geodin Acta 11(1):13–22

Montel JM (1993) A model for monazite/melt equilibrium and application to the generation of granitic magmas. Chem Geol 10:127–146

Müller W, Shelley M, Miller P, Broude S (2009) Initial performance metrics of a new custom-designed ArF excimer La-ICPMS system coupled to a two-volume laser-ablation cell. J Anal At Spectrom 24:209–214

Nicolas A, Bouchez JL, Blaise JL, Poirier JP (1977) Geological aspects of deformation in continental shear zones. Tectonophysics 42:55–73

Ourzik A, Debat P, Mercier A (1991) Metamorphic evolution of the N and Ne parts of the Montagne Noire Axial Zone (southern Massif-Central, France). C R Acad Sci Ser II 313(13):1547–1553

Pitra P, Poujol M, Van Den Driessche J, Poilvet JC, Paquette JL (2012) Early Permian extensional shearing of an Ordovician granite: the Saint-Eutrope "C/S-like" orthogneiss (Montagne Noire, French Massif Central). C R Geosci 34:377–384. doi:10.1016/j.crte.2012.06.002

Poilvet JC, Poujol M, Pitra P, Van Den Driesssche J, Paquette JL (2011) The Montalet granite, Montagne Noire, France: an Early Permian syn-extensional pluton as evidenced by new U–Th–Pb data on zircon and monazite. C R Geosci 343:454–461. doi:10.1016/j.crte.2011.06.002

Rabin M, Trap P, Carry N, Fréville K, Cenki-Tok B, Lobjoie C, Goncalves P, Marquer D (2015) Strain partitioning along the anatectic front in the Variscan Montagne Noire massif (Southern French Massif Central). Tectonics 34:1709–1735. doi:10.1002/2014TC003790

Rey PF, Teyssier C, Kruckenberg SC, Whitney DL (2011) Viscous collision in channel explains double domes in metamorphic core complexes. Geology 39(4):387–390

Rey PF, Teyssier C, Kruckenberg SC, Whitney DL (2012) Viscous collision in channel explains double domes inmetamorphic core complexes. Geology 40:e280 **(Forum Reply)**

Roger F, Respaut JP, Brunel M, Matte P, Paquette JL (2004) Première datation U–Pb des orthogneiss oeillés de la zone axiale de la Montagne Noire (Sud du Massif Central): nouveaux témoins du magmatisme ordovicien dans la chaîne varisque. C R Geosci Acad Sci Paris 336:19–28

Roger F, Maluski H, Lepvrier C, Van Vu T, Paquette JL (2012) LA-ICPMS zircons U/Pb dating of Permo–Triassic and Cretaceous magmatisms in Northern Vietnam—geodynamical implications. J Asian Earth Sci 48:72–82. doi:10.1016/j.jseaes.2011.12.012

Roger F, Teyssier Ch, Respaut JP, Rey P, Jolivet M, Whitney DL, Paquette JP, Brunel M (2015) Timing of deformation and exhumation of the Montagne Noire double dome, French Massif Central. Tectonophysics 640–641:53–69

Schuiling RD (1960) Le dome gneissique de l'Agoût (Tarn et Hérault). Mém Soc Géol Fr 91:59

Schulmann K, Edel JB, Hasalová P, Cosgrove J, Ježek J, Lexa O (2009) Influence of melt induced mechanical anisotropy on the magnetic fabrics and rheology of deforming migmatites, Central Vosges, France. J Struct Geol 31:1223–1237. doi:10.1016/j.jsg.2009.07.004

Soula JC, Debat P, Brusset S, Bessiere G, Christophoul F, Deramond J (2001) Thrust-related, diapiric, and extensional doming in a frontal orogenic wedge: example of the Montagne Noire, Southern French Hercynian belt. J Struct Geol 23(11):1677–1699. doi:10.1016/S0191-8141(01)00021-9

Steiger RH, Jäger E (1977) Subcommission on geochronology: convention on the use of decay constants in geo- and cosmochronology. Earth Planet Sci Lett 36:359–362

Thompson PH, Bard JP (1982) Isograds and mineral assemblages in the Eastern Axial Zone, Montagne Noire (France): implications for temperature gradients and P/T history. Can J Earth Sci 19(1):129–143

Van Den Driessche J, Brun JP (1989) Kinematic model of late Paleozoic extensional tectonics in the southern French massif central. C R Acad Sci II 309(16):1607–1613

Van Den Driessche J, Brun JP (1992) Tectonic evolution of the Montagne Noire (French Massif Central): a model of extensional gneiss dome. Geodin Acta 5:85–99

Van Den Driessche J, Pitra P (2012) Viscous collision in channel explains double domes in metamorphic core complexes. Geology 40(10):E279. doi:10.1130/G32727C.1

Vanderhaeghe O, Teyssier C (2001) Partial melting and flow of orogens. Tectonophysics 342:451–472

Vanderhaeghe O, Burg JP, Teyssier C (1999) Exhumation of migmatites in two collapsed orogens. In: Ring U, Brandon MT, Lister GS, Willet SD (eds) Exhumation processes: normal faulting, ductile flow and erosion, vol 154. Geological Society London Special Publications, London, pp 181–204

Whitney DL, Roger F, Teyssier Ch, Rey PF, Respaut JP (2015) Syn-collapse eclogite metamorphism and exhumation of deep crust in a migmatite dome/the P–T–t record of the youngest Variscan eclogite (Montagne Noire, French Massif Central). Earth Planet Sci Lett 430:224–234

Williams ML, Jercinovic MJ, Hetherington CJ (2007) Microprobe monazite geochronology: understanding geologic processes by integrating composition and chronology. Annu Rev Earth Planet Sci Lett 35:137–175